



**HAL**  
open science

## 3D printed tubular lattice metamaterials for mechanically robust stents

Huan Jiang, Hannah Ziegler, Zhennan Zhang, Heng Zhang, Louise Le Barbenchon, Sundar Atre, Yanyu Chen

► **To cite this version:**

Huan Jiang, Hannah Ziegler, Zhennan Zhang, Heng Zhang, Louise Le Barbenchon, et al.. 3D printed tubular lattice metamaterials for mechanically robust stents. *Composites Part B: Engineering*, 2022, 236, pp.109809. 10.1016/j.compositesb.2022.109809 . hal-03610888

**HAL Id: hal-03610888**

**<https://hal.science/hal-03610888>**

Submitted on 16 Mar 2022

**HAL** is a multi-disciplinary open access archive for the deposit and dissemination of scientific research documents, whether they are published or not. The documents may come from teaching and research institutions in France or abroad, or from public or private research centers.

L'archive ouverte pluridisciplinaire **HAL**, est destinée au dépôt et à la diffusion de documents scientifiques de niveau recherche, publiés ou non, émanant des établissements d'enseignement et de recherche français ou étrangers, des laboratoires publics ou privés.

## 3D printed tubular lattice metamaterials for mechanically robust stents

Huan Jiang<sup>1</sup>, Hannah Ziegler<sup>1</sup>, Zhennan Zhang<sup>1</sup>, Heng Zhang<sup>2,3</sup>, Louise Le Barbenchon<sup>4</sup>, Sundar Atre<sup>1</sup>, and

Yanyu Chen<sup>1\*</sup>

<sup>1</sup> Department of Mechanical Engineering, University of Louisville, Louisville, KY 40292, USA

<sup>2</sup> Department of Applied Mechanics and Aerospace Engineering, Waseda University, 3-4-1 Okubo, Shinjuku-ku, Tokyo 169-8555, Japan

<sup>3</sup> School of Mechanical Engineering, University of Shanghai for Science and Technology, Shanghai 200093, China

<sup>4</sup> Arts et Métiers ParisTech, CNRS, I2M Bordeaux, Esplanade des Arts et Métiers, Talence Cedex, F-33405, France

\*Corresponding author: Yanyu Chen (yanyu.chen@louisville.edu)

**Abstract:** Coronary artery disease (CAD) is the narrowing or blockage of the coronary arteries, usually caused by atherosclerosis. An interventional procedure using stents is a promising approach for treating CAD because stents can effectively open narrowed coronary arteries to improve blood flow to the heart. However, stents often suffer from catastrophic failures, such as fractures and migration of ligaments, resulting in fatal clinical events. In this work, we report a new type of tubular lattice metamaterial with enhanced mechanical resilience under radial compression, which can be used as an alternative for the current stent design. We begin by comparing the radial mechanical performance of the proposed auxetic tubular lattice (ATL) with the conventional diamond tubular lattice (DTL). Our results show that the ductility of ATL increases by 72.7% compared with that of the DTL structure. The finite element simulations reveal that the stress is more uniformly spread on the sinusoidal ligaments for ATL, while rather concentrated on the joints of straight ligaments for DTL. This phenomenon is intrinsically due to the bending of sinusoidal ligaments along both radial and axial directions, while straight beams bend mainly along the radial direction. We then investigated the effects of the geometrical parameters of the sinusoidal ligament on radial mechanical performance. Experimental results indicate that the beam depth  $h/l$  has the most significant effect on the stiffness and peak load. The stiffness

and maximum load surge by 789% and 1131%, respectively, when  $h/l$  increases from 0.15 to 0.30. In contrast, the beam amplitude  $A/l$  has a minor effect on the stiffness and peak load compared to beam depth and beam thickness. However, increasing the amplitude of the sinusoidal ligament can enlarge the ductility strikingly. The ductility can increase by 67.5% if the amplitude is augmented from  $A/l=0.1$  to  $A/l=0.35$ . The findings from this work can provide guidance for designing more mechanically robust stents for medical engineering.

**Keywords:** tubular structure; stents, metamaterials; ductility; 3D printing

## 1. Introduction

Heart disease is the leading cause of death in many developed countries, with coronary artery disease being the most common form of heart disease. Coronary artery disease (CAD) occurs when excess plaque accumulates in the cardiovascular arteries, resulting in narrowed arteries and restricted blood flow [1-3]. Cardiovascular stents are a non-surgical alternative to traditional treatment options and have become the most common interventional treatment for CAD [4, 5]. Stents are tubular structures that are implanted into obstructed arteries to expand the vessel and prevent arterial collapse. To be successful in clinical use, stents require high stretchability, bending flexibility, and radial strength [6]. Bending flexibility is vital for navigating stent placement and maintaining proper conformability while implanted [7, 8]. However, many conventional stents use straight ligaments, which restrict flexibility during deployment [9]. High radial strength is necessary for maintaining expansion in blocked arteries. Insufficient radial strength and bending flexibility in current stent designs have resulted in failure events such as stent collapse and migration [10-13]. Catastrophic failure of stent geometry also creates a risk of vessel perforation.

To overcome the limitations of existing stent designs, improvements to stent bending flexibility and radial strength have been explored. Stent radial strength is largely related to the mechanical properties of the base material and stent strut geometry [14]. As such, many studies have explored stent materials different from the original nitinol [15]. For example, composite metal-polymer braided stents have shown improved radial strength over braided nitinol

stents [16]. Thin membranes on the inner and outer surface of tubular structures have also been shown to increase the radial stiffness of traditional stent designs [17, 18]. More recently, biodegradable stent materials have been investigated for improved stent biocompatibility and bending flexibility, despite reduced radial strength compared to metal stents [19, 20]. Additionally, studies have explored the effects of changing geometric parameters on existing stent architectures. García et al. demonstrated control of stent radial stiffness through varied strut thickness and used these findings to develop a stent for variable radial force [21]. Strut geometry and connection type have also been used to vary stent bending flexibility [7, 20, 22]. In contrast to these commonly adopted methods, this research aims to develop new architectures to improve the radial behavior of tubular structures under large deformation.

Stent geometry has previously been limited by constraints of top-down fabrication methods. Due to the growing prevalence of additive manufacturing techniques, more complex tubular structures have been developed in recent years to address stent limitations [23-30]. For example, origami-inspired tubular structures have been studied for their improved producibility and versatility [31]. Foldable origami stents achieved favorable radial compressive strength using a single material, compared to dual material covered stents which risk incompatibility between stent and graft [32]. Tubular lattice structures have also been explored for their unique mechanical performance. For instance, the observed buckling response of cylindrical shell tubular lattices was highly non-linear and could be controlled through unit cell geometry [33]. Additionally, tubular auxetic materials have recently gained popularity for their novel behavior and tunable mechanical properties [34-39]. Auxetic materials exhibit a negative Poisson's ratio, which provides superior conformability during stent operation. Select microstructures exhibit auxetic behavior in compression, but not in tension, for wrinkle-free bending [40]. Controllable buckling response, bending flexibility, and torsional stiffness have also been investigated in tubular auxetics [23, 33, 40-42]. Mechanical performance of auxetics can be adjusted by modifying unit cell geometric parameters and base material, enabling stent customization.

There are very few studies focused on the radial compression behavior of tubular auxetics. Metallic Omega stent with helical connector design topology was investigated under radial compression and compared with shape memory

polymeric stent at different temperature scenarios [43]. It is reported that the radial strength hardly varies at the body temperature range and the metallic Omega stent shows higher radial force, indicating the effectiveness of supporting the arterial walls of vessel for the metallic Omega stent. However, this study is focused on the comparison of radial compression behavior for different materials, instead of considering the effect of the topology of stent. An auxetic vascular stent with arrowhead design was explored for the radial compression performance [44]. It is found that the increase of the wall thickness raises the ability of stent to resist radial deformation and the enlargement of stent diameter decreases the radial strength. However, their study did not explain how the auxetic effect contributes to the radial compression behavior.

In this work, we present a novel tubular lattice structure with auxetic unit cells for improved radial performance under large compressive deformation, and the mechanical response of the auxetic design was compared to a traditional, Palmaz-Schatz inspired, diamond lattice design [9] through a combined experimental and numerical approaches. Specifically, the finite element analyses (FEA) were conducted to provide additional insights for the mechanisms in the compressive deformation. As a novel contribution of this work, we proposed a newly designed Auxetic Tubular Lattice (ATL) structure and studied the effects of tubular lattice topology and the geometric parameters on the radial compression performance. In addition, we explained the auxetic effect on the radial compression behavior from numerical findings. Our experimental and numerical studies reveal the robust mechanical performance of the ATL structure.

## 2. Material and Methods

### 2.1 Tubular lattice metamaterials design

The design procedure of the proposed tubular metamaterial, namely auxetic tubular lattice (ATL), is illustrated in **Figs.1 (a)-(c)**. The 2D auxetic unit cell can be described by the parameters  $l$ ,  $t$  and  $A$ , where  $2l$  is the lattice constant of the unit cell,  $t$  is the thickness and  $A$  denotes the amplitude of the sinusoidal ligament. The 3D Representative Volume Element (RVE) consists of six bent 2D unit cells along the circumferential direction and one unit cell along

the axial direction. In the RVE,  $2l$  denotes the height,  $D$  represents the diameter of the circle,  $t$  and  $h$  denote the thickness and depth of the sinusoidal ligament, respectively. The 3D ATL model contains 11 RVEs along the axial direction. A 3D printed ATL is shown in **Fig. 1 (d)**. For comparison, we also designed a conventional tubular lattice as a benchmark, namely diamond tubular lattice (DTL). This structure is assembled using the same procedure, as shown in **Figs. 1 (e)-(g)**. DTL structure shares the same lattice constant  $2l$  and circle diameter  $D$  as ATL structure. To ensure the two configurations have the same mass, the thickness and depth of the beam are represented by different parameters  $p$  and  $q$ . A 3D printed DTL structure is shown in **Fig. 1 (h)**.

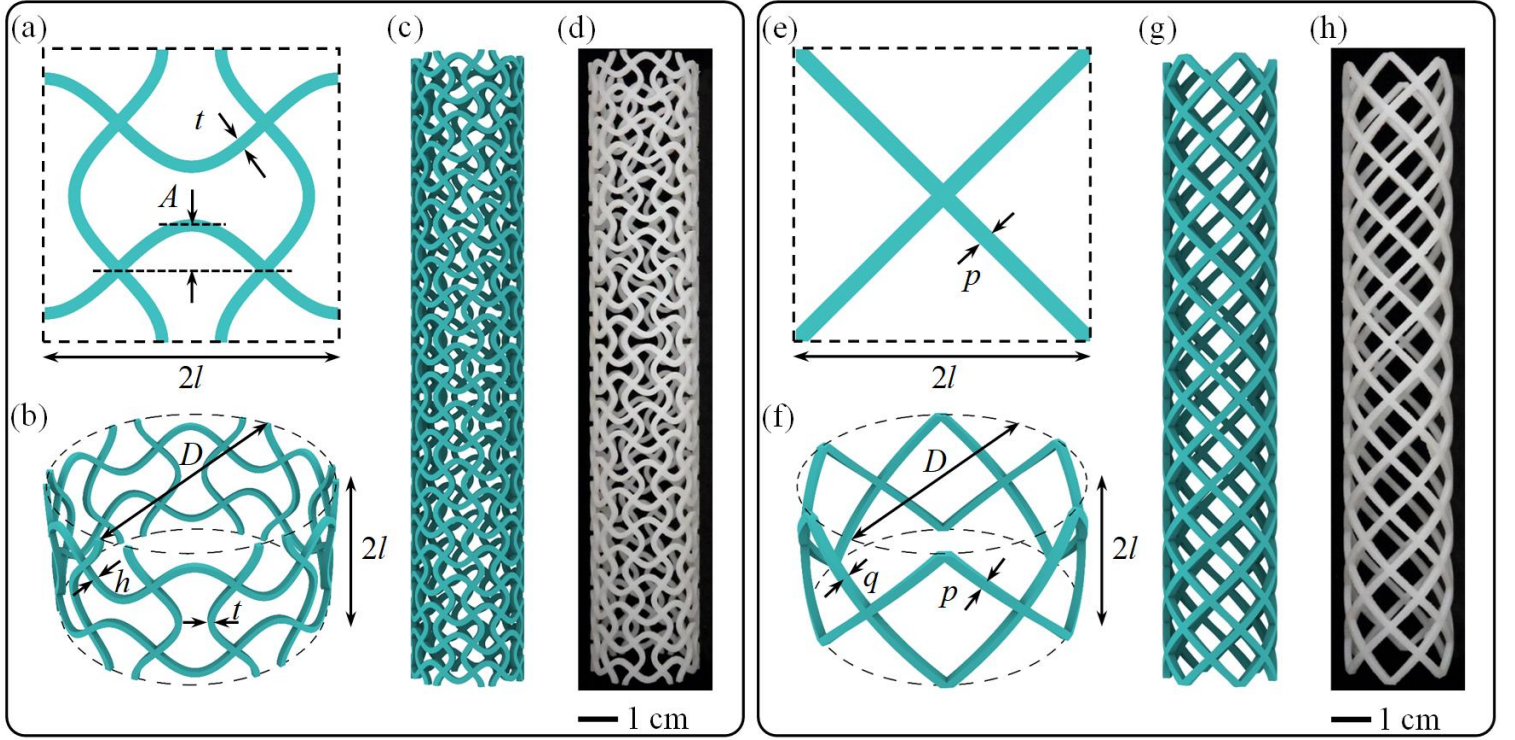


**Fig. 1.** Auxetic tubular lattice (ATL) and diamond tubular lattice (DTL) design. (a) 2D unit cell design of ATL.  $2l$  is the lattice constant of the unit cell,  $t$  is the thickness and  $A$  denotes the amplitude of sinusoidal ligament. (b) 3D Representative Volume Element (RVE) with six bent unit cells along the circumferential direction and one unit cell along the axial direction. Here,  $2l$  denotes the height of the RVE,  $D$  represents the diameter of the circle,  $t$  and  $h$  denote the thickness and depth of the sinusoidal ligament, respectively. (c) Geometrical model of ATL, with 11 RVEs

along the axial direction. (d) 3D printed sample of ATL. Here  $l = 7$  mm,  $D = 84/\pi$ ,  $A/l = 0.3$ ,  $t/l = 0.2$ ,  $h/l = 0.2$ . (e) 2D unit cell design of DTL.  $2l$  is the lattice constant of the unit cell,  $p$  is the thickness of the straight ligament. (f) 3D RVE with six unit cells along the circumferential direction and one unit cell along the axial direction. Here,  $2l$  denotes the height of the RVE,  $D$  is the diameter of the circle,  $p$  and  $q$  represent the thickness and depth of the beam, respectively. (g) Geometrical model of DTL, with 11 RVEs along the axial direction. (h) 3D printed sample of DTL. Here  $l = 7$  mm,  $D = 84/\pi$ ,  $p = q = 1.828$  mm.

## 2.2 Tubular lattice metamaterials fabrication

Polyjet additive manufacturing of photocurable resins is employed to fabricate the ATL and DTL structures. This technique enables the fabrication of complex structures with spatially varying geometry. CAD models of the tubular lattice structures were created using Rhinoceros® add-on Grasshopper (Robert McNeel & Associates, Seattle, USA). In this study, Object260 Connex Polyjet 3D printer (Stratasys Ltd., USA) is used for sample fabrication. This 3D printer employs polymer jetting technology which uses small nozzles to dispense liquid photopolymerizable monomer from a print head, which is then immediately cured by ultraviolet (UV) light using a source situated on-board of the printing head. With this printer, samples can be fabricated with a resolution of 16  $\mu\text{m}$  in the z-direction and 42  $\mu\text{m}$  in the x- and y-directions. Herein, a rigid polymer material, VeroWhitePlus, 1 is used to fabricate all the samples in a layer-by-layer fashion. A support material, SUP706, is used to improve the surface finish of the samples and to provide support for overhanging structures and can be removed by water jetting.

## 2.3 Radial compression testing

Quasi-static compression tests on ATL and DTL structures along radial direction are conducted using the Instron 5569A–Universal testing machine with a load cell of 50 kN. All samples are tested in displacement control mode at 3 mm/min with a final compression depth of 18 mm. The mechanical performance of the 3D printed specimens is first investigated by considering two geometric configurations (ATL and DTL). Then, the effects of beam depth  $h$ ,

thickness  $t$ , and amplitude  $A$  for ATL metamaterial are individually studied. An ARAMIS 4 M system (GOM GmbH, Germany) is used to capture deformations. Repeated testing is performed to ensure the reliability of the data. The effective stiffness, maximum load, and ductility are extracted from the measured load-displacement curve for each test.

## 2.4 Finite element simulation

Finite element simulations are conducted to provide additional insights into the compressive deformation mechanisms of the tubular lattice structures. The commercial software Abaqus/explicit (Providence, RI, USA) is employed for the simulations. **The elastic-perfectly-plastic constitutive model is adopted to simulate the VeroWhitePlus polymer. Tensile testing is performed per the ASTM standard [45] to obtain the material properties. The dumbbell-shape sample is shown in Fig. S1 (a), and the simplified constitutive model is shown in Fig. S1 (b). From the experimental data, we choose Young's modulus  $E = 1000$  MPa and yield strength is set to  $\sigma_y = 45$  MPa. Poisson's ratio  $\nu = 0.33$  is chosen from reference [46].** All tubular lattice structures are meshed with  $\sim 200,000$  C3D8 elements by using Hypermesh (Altair Engineering Inc., USA). The detailed finite element simulation setup is shown in **Fig. S1 (c) and (d)**. The convergence test is performed to eliminate the effect of mesh size. Meanwhile, the ratio of kinetic energy to the internal energy is controlled below 5% to get rid of the dynamic effect.

## 3. Results and discussion

### 3.1 Comparison between the proposed design and conventional design

To compare the proposed design and conventional design under compressive load, we performed compression tests on ATL and DTL samples. Each design was tested three times to eliminate the possibility of rare types of error that may be involved in these experiments. **Fig. 2 (a)** shows the load-displacement curves of ATL and DTL designs. Compared to the catastrophic failure of the DTL structure, the ATL exhibits a progressive failure mode. For the DTL structure, the load dropped significantly at a displacement of 4.8 mm, i.e., 88% loss of load. However, the ATL

structure showed no serious load drop during the process of compression, indicating a more ductile behavior. **Fig. 2 (b)** displays the comparison of stiffness, maximum load, and ductility of ATL and DTL designs. The ductility in this work was defined as the ratio of displacement at a 25% drop from the peak load to the maximum displacement, i.e., 18 mm. The error bars from repeated testing in **Fig. 2 (b)** show that the experiments repeated very well. Both stiffness and maximum load of ATL structure are smaller than that of DTL structure. However, the ductility of ATL increases by 72.7% compared to the DTL design.

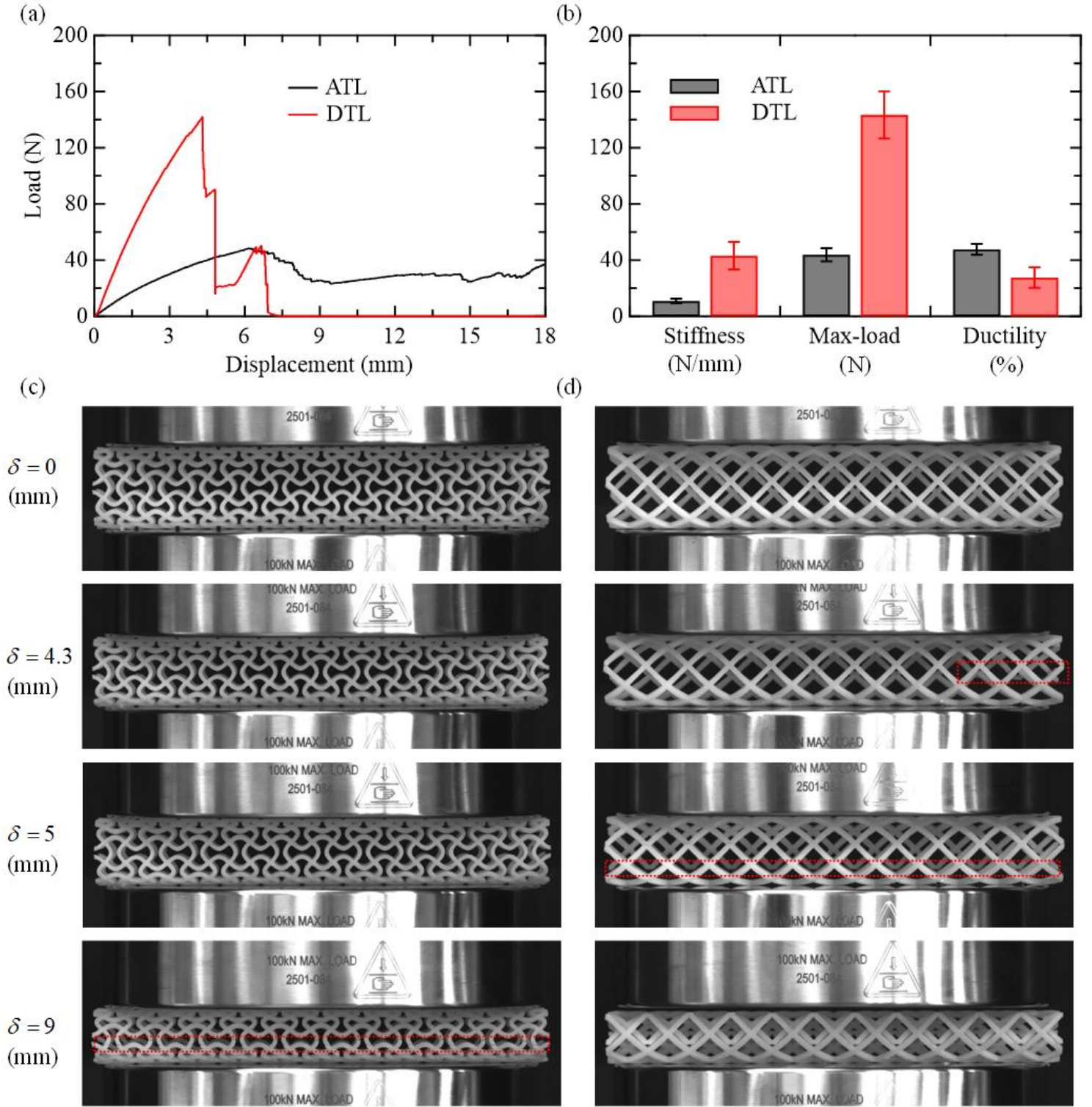


**Fig. 2.** Mechanical performance of ATL and DTL structures under compression. (a) Load-displacement curves for ATL and DTL. (b) Comparison of stiffness, maximum load, and ductility of ATL and DTL. (c) Deformation patterns

for ATL. Here,  $l = 7$  mm,  $D = 84/\pi$ ,  $A/l = 0.3$ ,  $t/l = 0.2$ ,  $h/l = 0.2$ . (d) Deformation patterns for DTL. Here,  $l = 7$  mm,  $R = 84/\pi$ ,  $p = q = 1.828$  mm.

**Figs. 2 (c)-(d)** display the deformation evolutions of ATL and DTL structures under different displacements. At the displacement of  $\delta = 4.3$  mm, the ATL design shows no observable failure. However, the DTL design breaks at the joints of straight beams, as highlighted in the image. This failure corresponds to the load drop in the load-displacement curve. At the displacement of  $\delta = 5$  mm, ATL structure still shows no observable failure, while DTL design exhibits complete dislocation at the joints, highlighted in the image across the sample. This contributes to the further load drop of 88% in the load-displacement curve. As the displacement rises to  $\delta = 9$  mm, fractures are generated in the ATL structure, shown in the highlighted region. However, the integrity of the ATL structure is not affected despite these fractures, indicating a remarkably ductile performance. On the other hand, the DTL design is characterized by a complete dislocation at multiple joints, leading to the total collapse of the specimen. This explains the plummet of load to zero.

To gain further insights into the mechanisms that are responsible for the disparate deformations of ATL and DTL structures, finite element simulations were performed. The simulated and measured load-displacement curves for ATL and DTL structures are shown in **Figs. 3 (a)** and **(b)**, respectively. The simulations were conducted to reveal the mechanisms before fracture. Therefore, we did not consider the failure in our simulations. **Figs. 3 (c)** and **(d)** show the Mises stress contour plots of ATL and DTL structures under different compressive displacements. One can observe that the Mises stress for the ATL structure is more uniformly distributed on the circumferential ligaments, while the stress for DTL design is rather concentrated on the joints of straight ligaments. It is also interesting to see that the axial sinusoidal ligaments of the ATL structure do not significantly contribute to bearing the load. The detailed distribution of stress components for ATL and DTL design is shown in **Fig. S2** in the Supplementary Information (SI). **Figs. S2 (a)** and **(b)** display the  $\sigma_{xx}$  for the ATL and DTL structures, respectively. It is apparent that the stress component  $\sigma_{xx}$

is largely distributed on the circumferential ligaments in the middle region between the top and bottom plates for ATL design, and mostly concentrated on the joints for the DTL design. The stress component  $\sigma_{yy}$  is widely distributed on the circumferential ligaments close to the top and bottom plates, while mainly concentrated on the joints near the top and bottom plate. On the other hand, the stress component  $\sigma_{zz}$  is primarily spread on the axial ligaments along the sample for ATL. However, the magnitude of  $\sigma_{zz}$  is significantly smaller compared to  $\sigma_{xx}$ . Furthermore, the contour plot of displacement along the axial direction shown in **Figs. S2 (g) and (h)** reveals an auxetic effect, which shows that the sinusoidal ligaments flow toward the inside of the ATL structure, while the straight beams flow toward the outside of the DTL structure. This unique feature leads to the bending of circumferential sinusoidal ligaments along both radial and axial directions. However, the straight ligaments of the DTL structure bend along the radial direction.

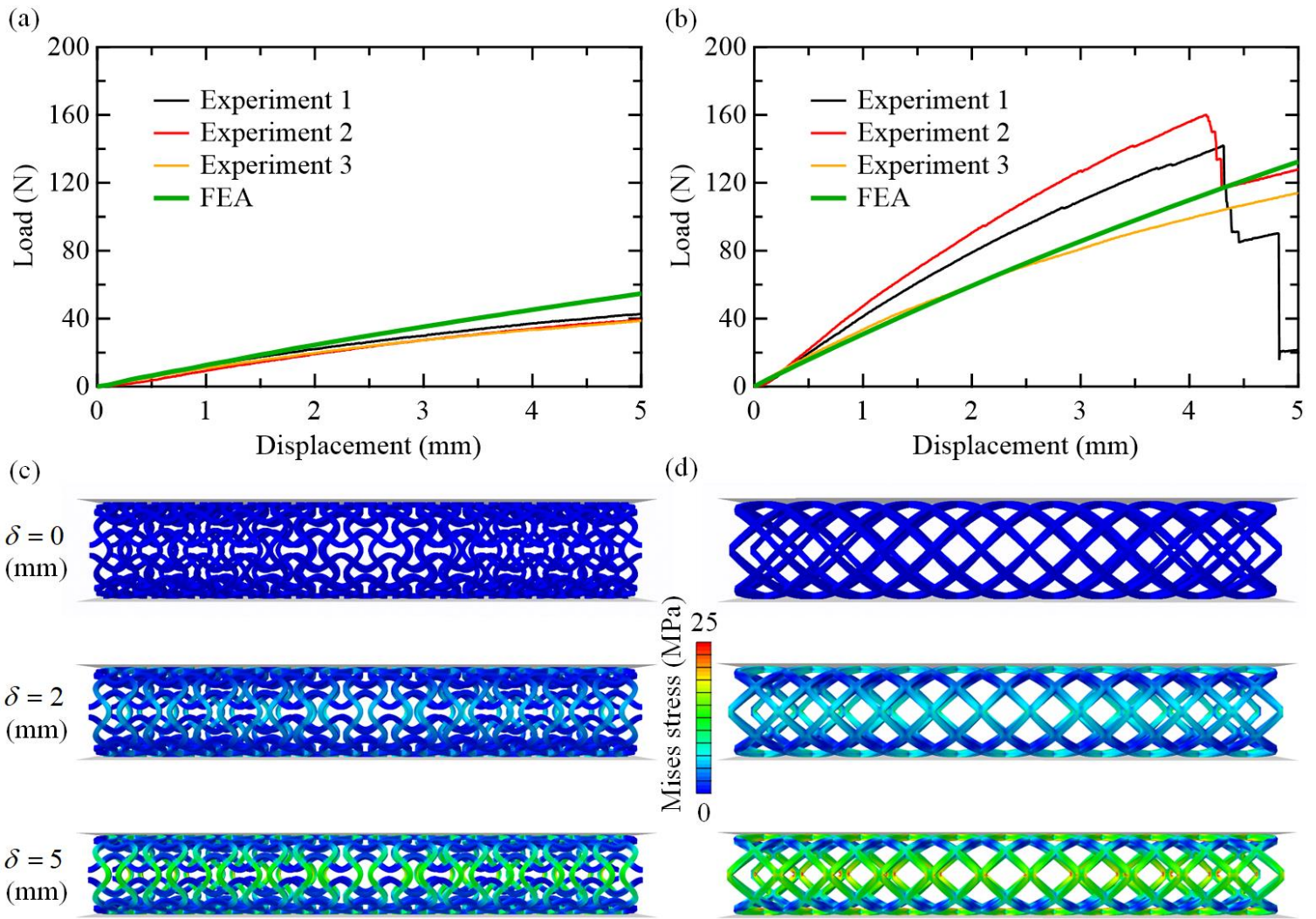


**Fig. 3.** Finite element simulations for ATL and DTL structures. (a) Measured and simulated load-displacement curves for ATL structure. (b) Measured and simulated load-displacement curves for DTL structure. (c) Mises stress contour plots for ATL. (d) Mises stress contour plots for DTL.

For vascular stents, radial strength is a primary design requirement to withstand compressive forces exerted by the vascular wall. On the one hand, insufficient radial strength during the revascularization and early stage of restoration causes acute elastic recoil of the artery and frequent migration [47, 48]. On the other hand, the catastrophic failure of stent could induce protrusion into the vessel lumen and trigger platelet activation [49], which poses serious threat to patients. Therefore, the stent with sufficient radial strength and the capacity to prevent catastrophic failure

are required as the ideal candidate for clinical usage. In the above investigation, we demonstrate that although the DTL structure displays higher radial strength than that of the ATL architecture, it suffers from disastrous collapse once the radial strength is reached. The ATL design shows more ductility than the DTL one, which indicates the small amount of radial strength drop after the peak point. Note that the overall radial strength of ATL is comparatively smaller than DTL. To demonstrate the advantage of ATL design, we will show the tunability of radial strength for ATL design without sacrificing its ductility by performing parametric analyses.

### 3.2 Effect of beam depth

Having studied the mechanical performance of the proposed tubular lattice architecture, we proceed to demonstrate the design flexibility of ATL design by altering the geometric parameters of the sinusoidal ligament, including beam depth  $h$ , beam thickness  $t$ , and beam amplitude  $A$ . We start by investigating the effect of beam depth  $h/l$  on mechanical performance. The shape evolution for different beam depths is shown in **Fig. 4 (a)**. The measured load-displacement relations for different beam depths are displayed in **Fig. 4 (b)**. One can observe that the load drop is increasingly significant with the enlargement of beam depth, indicating a more brittle failure mode for large beam depth. As summarized in **Figs. 4 (c) and (d)**, both the stiffness and maximum load show an increasing trend with the augment of beam depth. Particularly, the stiffness and maximum load surge by 789% and 1131%, respectively, when  $h/l$  increases from 0.15 to 0.30. **Fig. 4 (e)** displays the ductility of the ATL structure with various beam depths. The ductility for different beam depth models remains relatively high, i.e., ~40%, compared with what we reported for DTL design.

**Figs. 5 (a) and (b)** display the deformation patterns for ATL design with  $h/l = 0.15$  and  $h/l = 0.30$ , respectively. For the convenience of description, we will use the model parameter to represent the model throughout the work. For instance, we use  $h/l = 0.15$  to denote the ATL structure with  $h/l = 0.15$ . At the displacement of  $\delta = 7.1$  mm,  $h/l = 0.15$  shows fractures in the middle region, as highlighted in the image. The  $h/l = 0.30$ , on the other hand, exhibits

fewer fractures in the highlighted area at this stage. However, the load drop for  $h/l = 0.30$  is more rapid than that of  $h/l = 0.15$  as seen from the load-displacement curves in **Fig. 4 (b)**, indicating the catastrophic failure of  $h/l = 0.30$ . At the displacement of  $\delta = 10$  mm,  $h/l = 0.15$  shows a similar fracture pattern to the previous stage, and the sample maintains the integrity of the structure. In contrast, disastrous failure occurs at this point for  $h/l = 0.30$ , as can be observed from the image where the highlighted part breaks off from the sample. This observation verifies our previous description of catastrophic failure for  $h/l = 0.30$ .

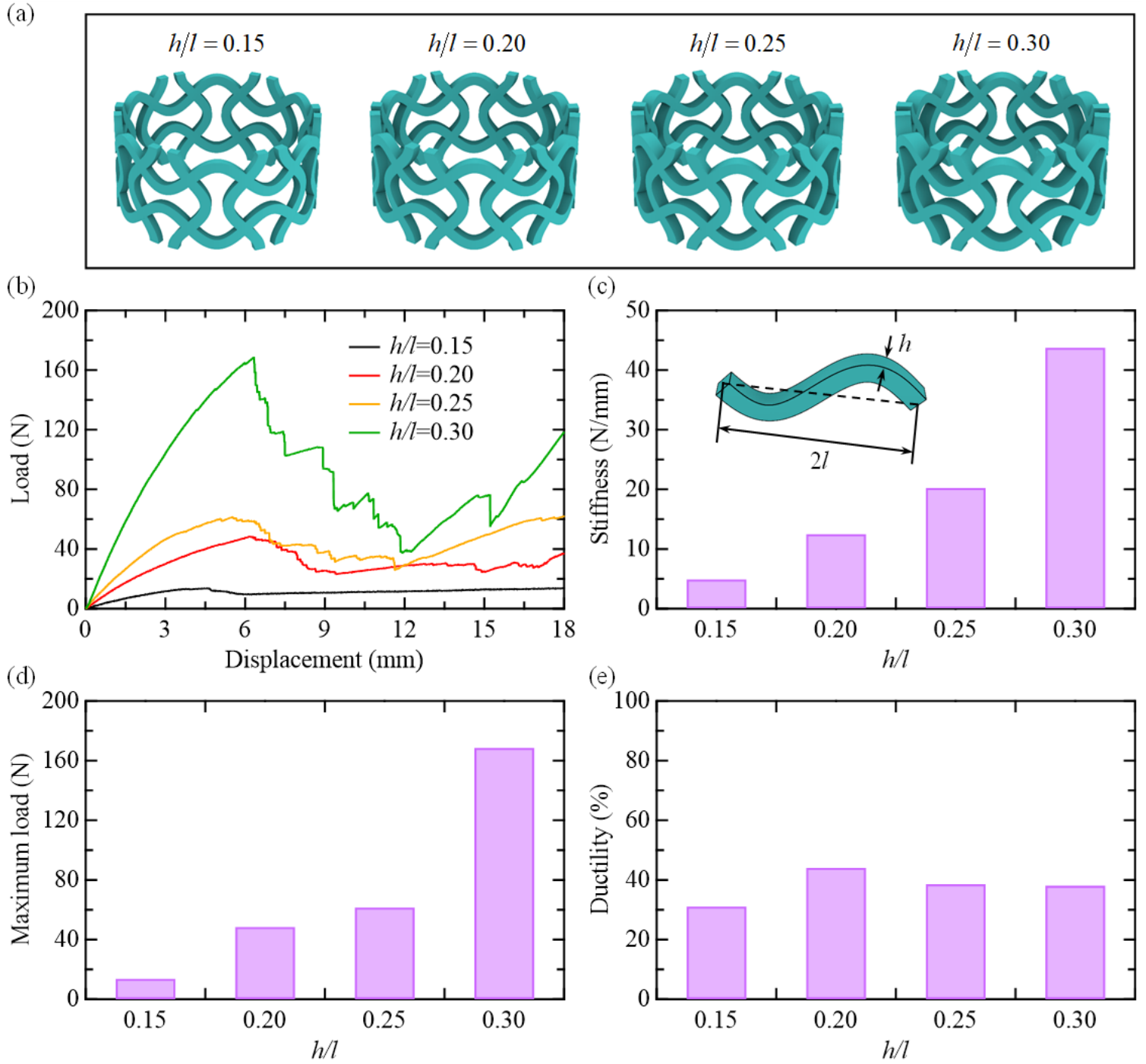


**Fig. 4.** Effect of beam depth on the performance of ATL structure. (a) RVEs with different beam depths. (b) Load-displacement curves. (c) Tubular lattice stiffness as a function of  $h/l$ . (d) Tubular lattice maximum load as a function of  $h/l$ . (e) Tubular lattice ductility as a function of  $h/l$ . Here,  $l = 7$  mm,  $D = 84/\pi$ ,  $A/l = 0.3$ ,  $t/l = 0.2$ .

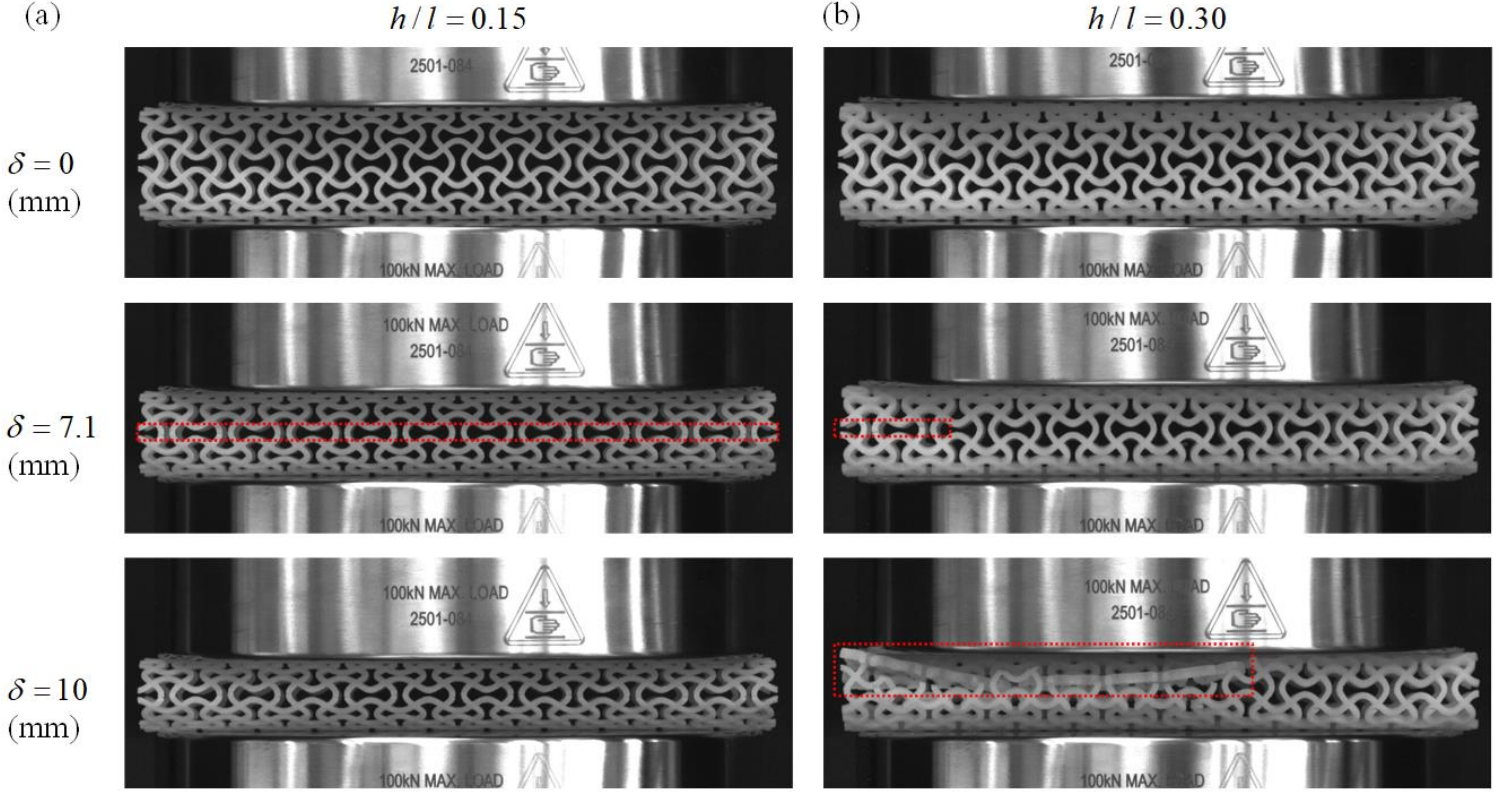


**Fig. 5.** Comparison of deformation patterns for ATL structure with different beam depths. (a) Deformation patterns for  $h/l = 0.15$ . (b) Deformation patterns for  $h/l = 0.30$ .

### 3.3 Effect of beam thickness

In this section, we proceed to investigate the effect of beam thickness  $t$  on the mechanical performance of the ATL structure. RVEs with different beam thicknesses are schematically shown in **Fig. 6 (a)**. The load-displacement curves for different beam thicknesses are shown in **Fig. 6 (b)**. One can observe that the ATL structure tends to exhibit a more brittle failure phenomenon with the increase of beam thickness  $t$ , similar to the effect of beam depth  $h$ . **Figs. 6 (c) and (d)** display stiffness and maximum load for various beam thickness models. The stiffness and maximum load are enhanced by 241% and 231%, respectively, when the beam thickness enlarges from  $t/l = 0.15$  to  $t/l = 0.30$ . This indicates that the contribution of beam thickness is significantly smaller compared to that of beam depth. This phenomenon can be intrinsically explained by analogy to beam theory. For the compression case in our work, the

bending stiffness of the sinusoidal ligaments can be expressed by  $M = CE\kappa th^3$  [50]. Here,  $C$  is the geometric constant,  $E$  is Young's modulus, and  $\kappa$  is the curvature. Therefore, beam depth  $h$  has a more important role than beam thickness  $t$  in this scenario. **Fig. 6 (e)** shows the ductility of ATL design with different beam thicknesses. Ductility for all the studied samples was relatively high, i.e., ~40%, indicating a superior compliant behavior compared to the DTL structure.

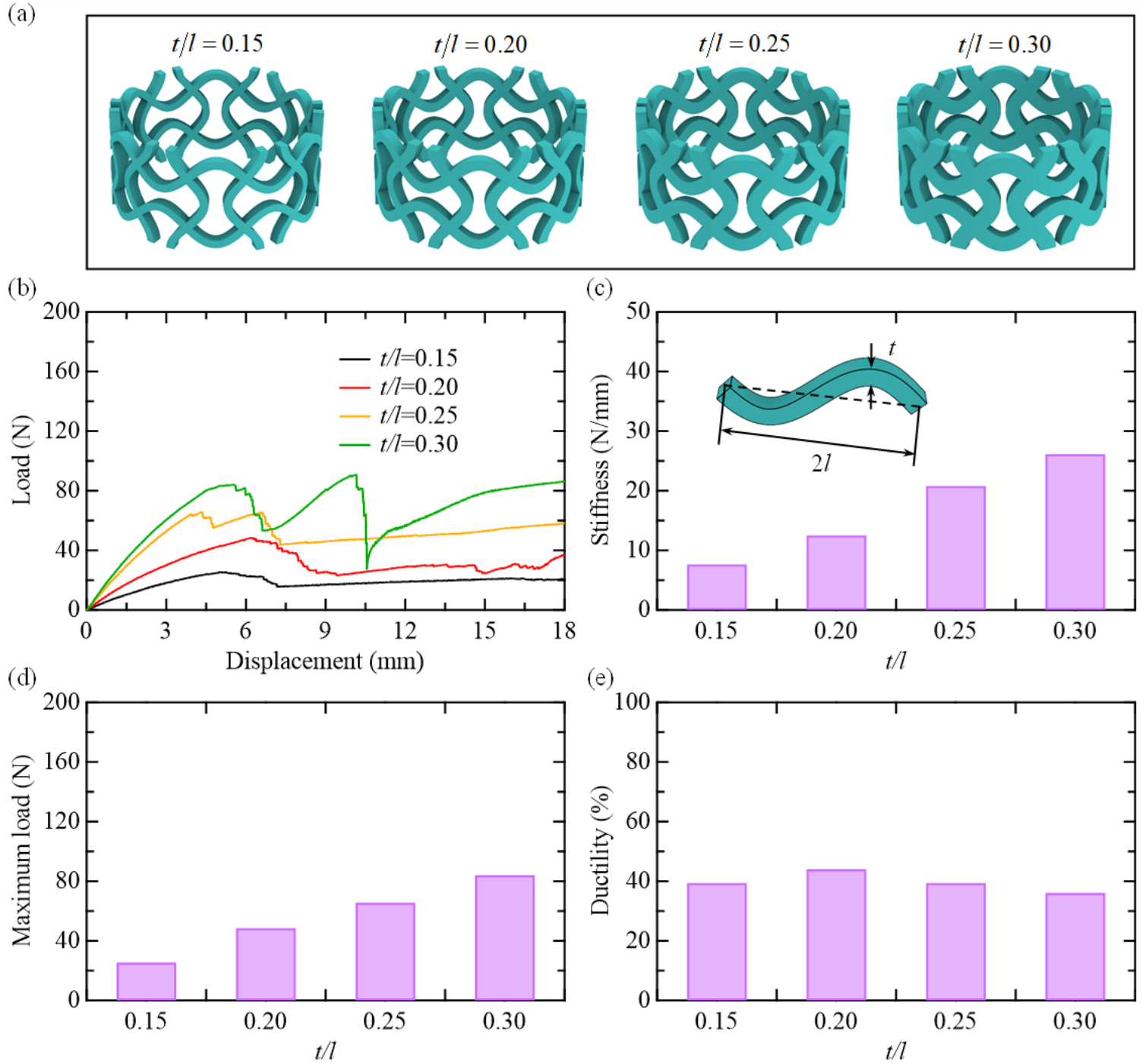


**Fig. 6.** Effect of beam thickness on the performance of ATL structure. (a) RVEs with different beam thicknesses. (b) Load-displacement curves. (c) Tubular lattice stiffness as a function of  $t/l$ . (d) Tubular lattice maximum load as a function of  $t/l$ . (e) Tubular lattice ductility as a function of  $t/l$ . Here,  $l = 7$  mm,  $D = 84/\pi$ ,  $A/l = 0.3$ ,  $h/l = 0.2$ .

**Figs. 7 (a)** and **(b)** show the deformation evolutions for  $t/l=0.15$  and  $t/l=0.30$ , respectively. At the displacement of  $\delta = 7$  mm, we can observe multiple fractures for  $t/l=0.15$  in the region highlighted in the image. A similar fracture pattern happened for  $t/l=0.30$  as well, as shown in the highlighted region. However, the difference is that the load drops due to the ligament failure for  $t/l=0.30$  is much more rapid than that of  $t/l=0.15$ , as seen in the load-displacement relation in **Fig. 6 (b)**. This indicates a more brittle failure for a larger beam thickness model. At the displacement of  $\delta = 10.6$  mm,  $t/l=0.15$  exhibits analogous fracture pattern to the previous stage. On the other hand,  $t/l=0.30$  displays a significantly different failure manner. The symmetry of the model has been completely destroyed, which can be seen by looking at the holes highlighted in the image. Meanwhile, a considerable load plummet occurs at this point. These facts indicate a catastrophic failure of  $t/l=0.30$  at this stage.

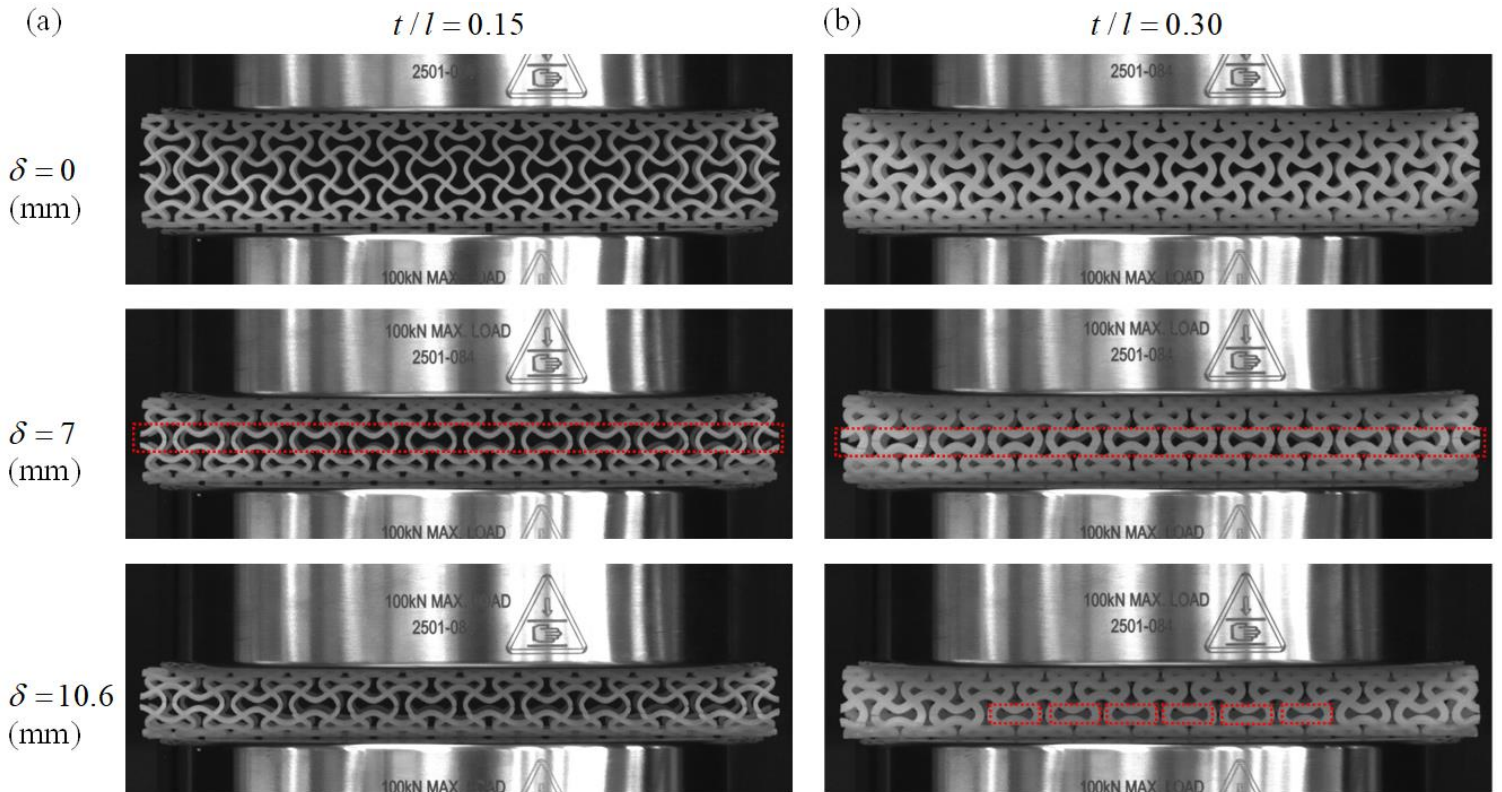


**Fig. 7.** Comparison of deformation patterns for ATL structure with different beam thickness. (a) Deformation patterns for  $t/l = 0.15$ . (b) Deformation patterns for  $t/l = 0.30$ .

### 3.4 Effect of beam amplitude

In this part, we proceed to investigate the effect of beam amplitude on the mechanical performance of the ATL structure. The RVEs with different beam amplitudes are shown in **Fig. 8 (a)**. The load-displacement relation curves for different beam amplitudes are shown in **Fig. 8 (b)**. Stiffness shows a decreasing trend with the increase of the beam amplitude, and the finite element simulation results in the inset verify this finding. Furthermore, the yield load occurs at larger displacement when the beam amplitude becomes bigger, indicating a more compliant behavior. **Figs. 8 (c) and (d)** display the category plot of stiffness and maximum load, respectively. The stiffness exhibits a decreasing trend with increasing amplitude as observed from the load-displacement curves. Particularly, the stiffness is reduced by 61.5% when the amplitude is enlarged from  $A/l = 0.1$  to  $A/l = 0.35$ . On the other hand, the maximum load does not show a pattern due to the randomness of failure. Quite interestingly, the beam amplitude is found to have a less significant effect on the load-displacement response than beam thickness and depth. This is different from what we reported in the tensile testing in our previous work [50]. **Fig. 8 (e)** shows the ductility of ATL design with various beam amplitude. The ductility is discovered to exhibit an increasing trend with the augment of beam amplitude. To further investigate the mechanism behind this phenomenon, we show the contour plot of Mises stress for different beam amplitude models in **Fig. S3**. As one increases the amplitude, a more uniform stress distribution is observed. For  $A/l = 0.10$  in **Fig. S3 (a)**, the stress is slightly concentrated on the middle part of the circumferential ligaments. However, the local concentrated regions dissipate gradually as the beam amplitude enlarges, as shown in **Figs. S3 (b) and (c)**. This attributes to the auxetic effect which we have discussed in section 3.1. The circumferential ligaments bend mainly along the radial direction due to the little auxetic effect when the beam amplitude is small. In contrast, the notable auxetic effect will compel the circumferential ligaments to bend along both radial direction and axial

direction as the beam amplitude increases. Particularly, the ductility is enhanced by 225% if the beam amplitude is enlarged from  $A/l=0.1$  to  $A/l=0.35$ , where the  $A/l=0.35$  displays ductility up to 67.5%.

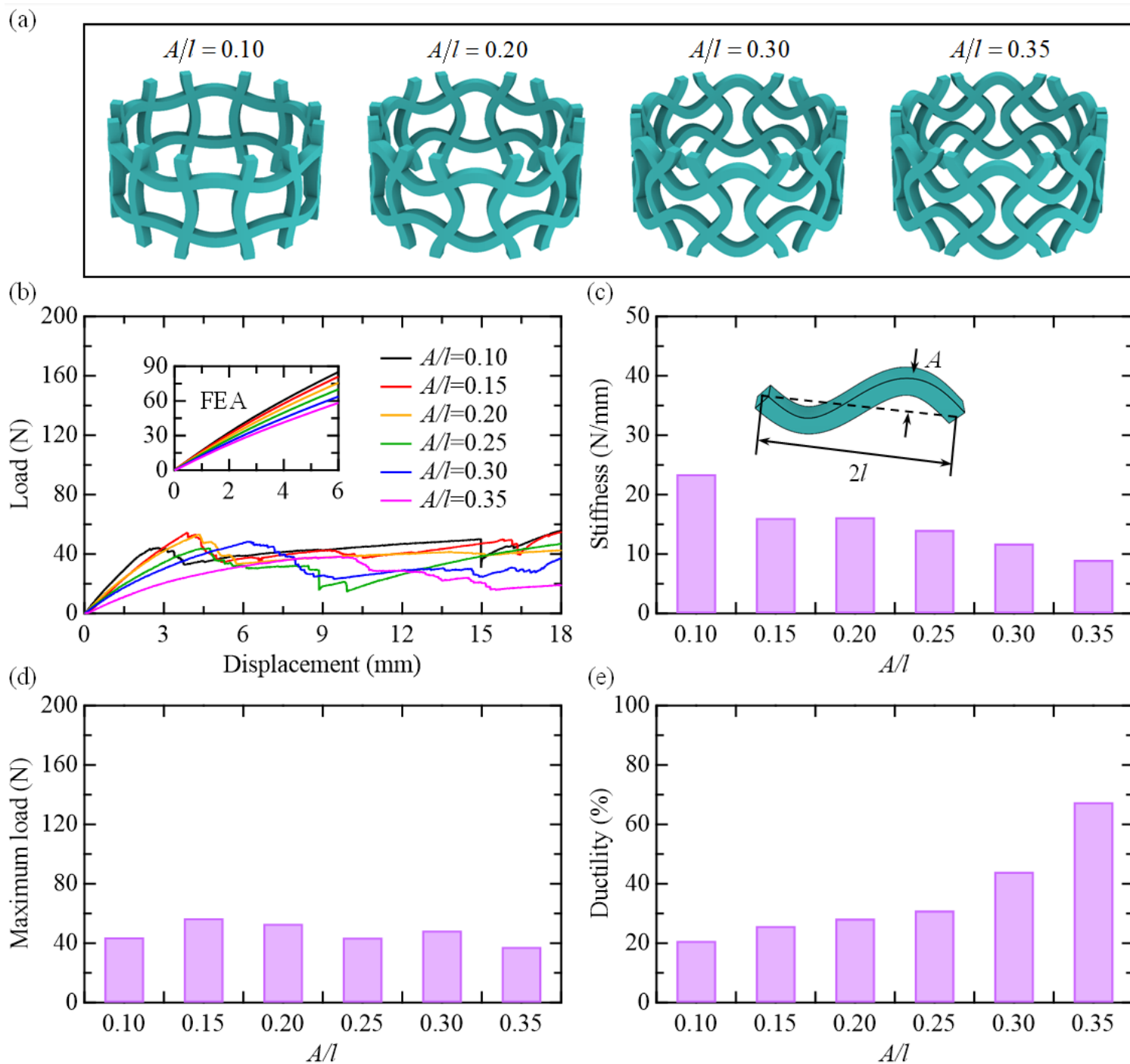


**Fig. 8.** Effect of amplitude on the performance of ATL. (a) RVEs with different beam amplitude. (b) Load-displacement curves. (c) Tubular lattice stiffness as a function of  $A/l$ . (d) Tubular lattice maximum load as a function of  $A/l$ . (e) Tubular lattice ductility as a function of  $A/l$ . Here,  $l = 7$  mm,  $D = 84/\pi$ ,  $t/l = 0.2$ ,  $h/l = 0.2$ .

**Figs. 9 (a) and (b)** show the deformation patterns for  $A/l = 0.1$  and  $A/l = 0.35$ , respectively. At the displacement of  $\delta = 3$  mm, fractures occur on the ligaments for  $A/l = 0.1$  as highlighted in the image, which accounts for the load drop in the load-displacement curve. However, no observable failure is found for  $A/l = 0.35$  at this stage, as evidenced by the smooth rising of load. At the displacement of  $\delta = 10$  mm, the fracture grows significantly. On the other hand,  $A/l = 0.35$  shows only mild failure, as shown in the highlighted area. This indicates significant ductile behavior of  $A/l = 0.35$ .

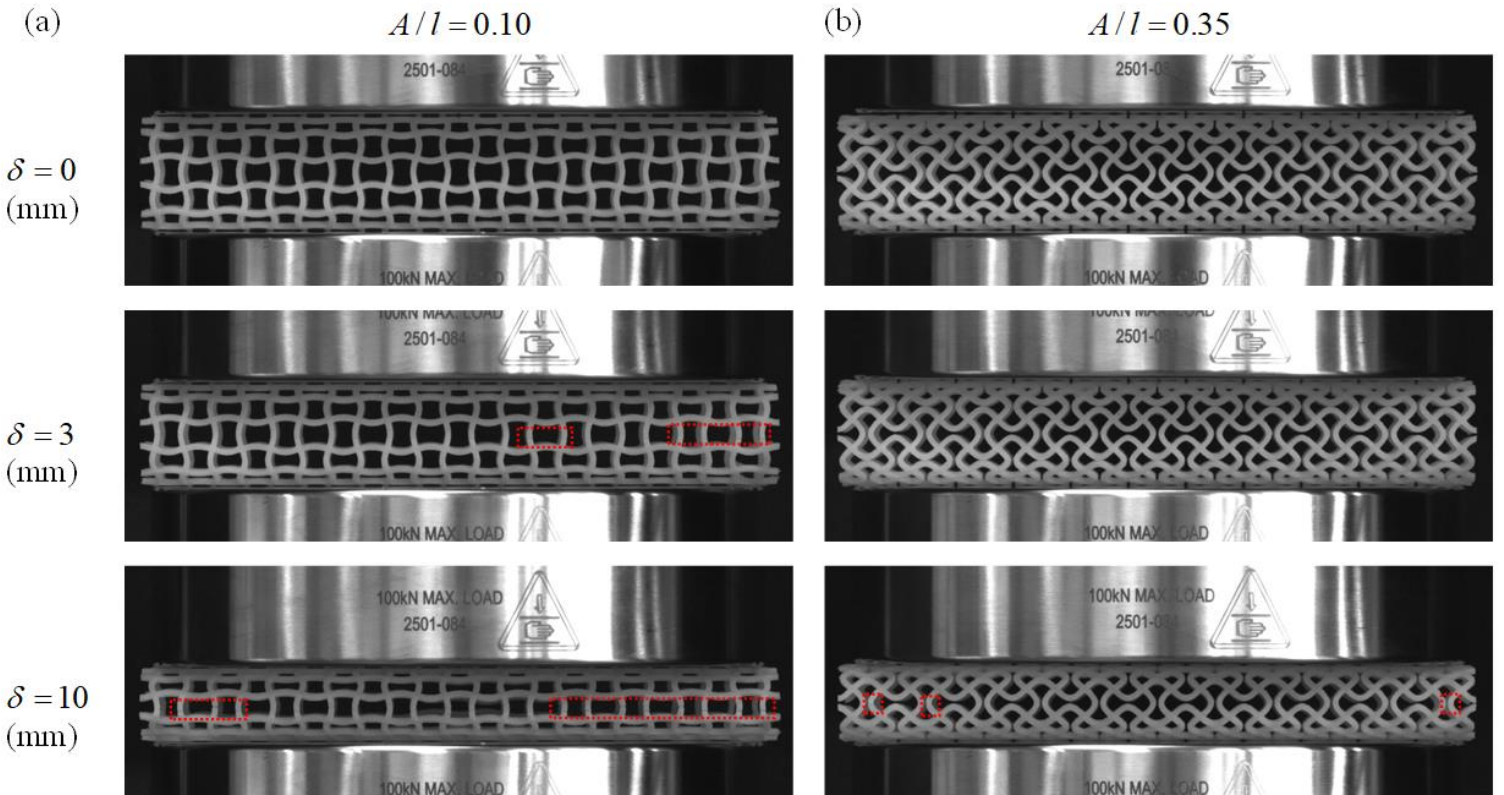


**Fig. 9.** Comparison of deformation patterns for ATL structure with different beam amplitudes. (a) Deformation patterns for  $A/l = 0.1$ . (b) Deformation patterns for  $A/l = 0.35$ .

#### 4. Conclusions

In summary, we have investigated the mechanical performance of a newly developed tubular lattice metamaterial under radial compression using an integrated experimental and numerical effort. Compared with conventional DTL structure, the proposed ATL design has superior ductility under large deformation. Our numerical simulations revealed the disparate stress distributions within the two configurations. The stress is concentrated on the joints of straight beams for DTL structure, while stress is more uniformly distributed on the sinusoidal ligaments for ATL structure. Intrinsically, this is due to the bending of sinusoidal ligaments along both radial and axial directions, which features more deformation space. In contrast, the straight beams are bent mainly along the radial direction. To explore the design flexibility of the proposed lattice metamaterials, we investigated the geometric features of beam ligament on the mechanical performance. We found that the beam depth  $h/l$  significantly affects the stiffness and peak load, while beam amplitude  $A/l$  influences the ductility extraordinarily. These parametric analyses can enable us to design ATL structures with prescribed radial performance, such as stiff yet ductile features. **It should be pointed out, though, that we did not maintain the same relative density for the samples in the parametric studies. The difference of relative density will affect the relative values of mechanical properties. However, this difference has no effect in our findings and conclusions. As a preliminary study, we anticipate the proposed mechanically robust tubular architectures can be used as stents that will have a high potential for clinical translation to treat coronary and peripheral artery disease. Our ongoing work includes evaluation of the mechanical performance of this tubular lattice architecture with degradable constitutive materials and further optimizing the tubular architecture using inverse design approaches.**

#### Author statement

Huan Jiang: Methodology, Formal analysis, Investigation, Data Curation; Hannah Ziegler, Zhennan Zhang, Heng Zhang, and Louise Le Barbenchon: Investigation, Data Curation, Writing - Original Draft; Sundar Atre and Yanyu Chen: Conceptualization, Writing - Review & Editing, Supervision. All authors have approved the final version of the manuscript.

## **Acknowledgments**

YC gratefully acknowledges the start-up fund from the Department of Mechanical Engineering at the University of Louisville.

## **Declaration of competing interest**

The authors declare that they have no known competing financial interests or personal relationships that could have appeared to influence the work reported in this paper.

## **Data availability**

The raw/processed data required to reproduce these findings cannot be shared at this time due to technical or time limitations.

## **References**

- [1] Hannan EL, Racz MJ, Arani DT, McCallister BD, Walford G, Ryan TJ. A comparison of short- and long-term outcomes for balloon angioplasty and coronary stent placement. *J. Am. Coll. Cardiol.* 2000;36(2):395-403.
- [2] Bart L, Dolmatch UB. Stent-Grafts: Current Clinical Practice. *Radiology.* 2000;217(1):94-94.
- [3] Wu W, Song X, Liang J, Xia R, Qian G, Fang D. Mechanical properties of anti-tetrachiral auxetic stents. *Compos. Struct.* 2018;185:381-92.
- [4] Palmaz JC. Balloon-expandable intravascular stent. *AJR.* 1988;150(6):1263-9.
- [5] Spencer B, King BM. Interventional Treatment of Coronary Heart Disease and Peripheral Vascular Disease. *Circulation.* 102(suppl\_4):Iv-81-Iv-6.
- [6] Wang Q, Fang G, Zhao Y-H, Zhou J. Improvement of Mechanical Performance of Bioresorbable Magnesium Alloy Coronary Artery Stents through Stent Pattern Redesign. *Appl. Sci.* 2018;8(12).
- [7] Shi W, Li H, Zhu T, Jin Y, Wang H, Yang J, et al. Study on the bending behavior of biodegradable metal cerebral vascular stents using finite element analysis. *J. Biomech.* 2020;108:109856.
- [8] Demanget N, Latil P, Orgéas L, Badel P, Avril S, Geindreau C, et al. Severe bending of two aortic stent-grafts: an experimental and numerical mechanical analysis. *Ann. Biomed. Eng.* 2012;40(12):2674-86.
- [9] Butany J, Carmichael K, Leong SW, Collins MJ. Coronary artery stents: identification and evaluation. *J. Clin. Pathol.* 2005;58(8):795-804.

- [10] Wong P, Leung WH, Wong CM. Migration of the AVE Micro coronary stent. *Catheter. cardiovasc. diagnosis.* 1996;38(3):267-73.
- [11] McGrath DJ, O'Brien B, Bruzzi M, McHugh PE. Nitinol stent design – understanding axial buckling. *J. Mech. Behav. Biomed. Mater.* 2014;40:252-63.
- [12] Grogan JA, Leen SB, McHugh PE. Computational micromechanics of bioabsorbable magnesium stents. *J. Mech. Behav. Biomed. Mater.* 2014;34:93-105.
- [13] Jacobs TS, Won J, Gravereaux EC, Faries PL, Morrissey N, Teodorescu VJ, et al. Mechanical failure of prosthetic human implants: a 10-year experience with aortic stent graft devices. *J. Vasc. Surg. Cases.* 2003;37(1):16-26.
- [14] Dumoulin C, Cochelin B. Mechanical behaviour modelling of balloon-expandable stents. *J. Biomech.* 2000;33(11):1461-70.
- [15] Cockerill I, See CW, Young ML, Wang Y, Zhu D. Designing Better Cardiovascular Stent Materials: A Learning Curve. *Adv. Funct. Mater.* 2021;31(1):2005361.
- [16] Zheng Q, Dong P, Li Z, Han X, Zhou C, An M, et al. Mechanical characterizations of braided composite stents made of helical polyethylene terephthalate strips and NiTi wires. *Nanotechnol. Rev.* 2019;8(1):168-74.
- [17] McGrath DJ, O'Brien B, Bruzzi M, Kelly N, Clauser J, Steinseifer U, et al. Evaluation of cover effects on bare stent mechanical response. *J. Mech. Behav. Biomed. Mater.* 2016;61:567-80.
- [18] Shang Z, Ma J, You Z, Wang S. Lateral indentation of a reinforced braided tube with tunable stiffness. *Thin-Walled Struct.* 2020;149:106608.
- [19] Grogan JA, Leen SB, McHugh PE. Comparing coronary stent material performance on a common geometric platform through simulated bench testing. *J. Mech. Behav. Biomed. Mater.* 2012;12:129-38.
- [20] Wang L, Chan Y-C, Liu Z, Zhu P, Chen W. Data-driven metamaterial design with Laplace-Beltrami spectrum as “shape-DNA”. *Struct. Multidisc. Optim.* 2020;61(6):2613-28.
- [21] García A, Peña E, Martínez MA. Influence of geometrical parameters on radial force during self-expanding stent deployment. Application for a variable radial stiffness stent. *J. Mech. Behav. Biomed. Mater.* 2012;10:166-75.
- [22] Han Y, Lu W. Optimizing the deformation behavior of stent with nonuniform Poisson's ratio distribution for curved artery. *J. Mech. Behav. Biomed. Mater.* 2018;88:442-52.
- [23] Lei M, Hong W, Zhao Z, Hamel C, Chen M, Lu H, et al. 3D Printing of Auxetic Metamaterials with Digitally Reprogrammable Shape. *ACS Appl. Mater. Interfaces.* 2019;11(25):22768-76.
- [24] Paxton NC, Daley R, Forrestal DP, Allenby MC, Woodruff MA. Auxetic tubular scaffolds via melt electrowriting. *Mater. Des.* 2020;193:108787.
- [25] Leonardi F, Graziosi S, Casati R, Tamburrino F, Bordegoni M. Additive Manufacturing of Heterogeneous Lattice Structures: An Experimental Exploration. *Proc. Int. Conf. Eng. Des.* 2019;1(1):669-78.
- [26] Cabrera MS, Sanders B, Goor OJGM, Driessen-Mol A, Oomens CWJ, Baaijens FPT. Computationally Designed 3D Printed Self-Expandable Polymer Stents with Biodegradation Capacity for Minimally Invasive Heart Valve Implantation: A Proof-of-Concept Study. *3D Printing and Addit. Manuf.* 2017;4(1):19-29.
- [27] Zaccaria A, Pennati G, Petrini L. Analytical methods for braided stents design and comparison with FEA. *J. Mech. Behav. Biomed. Mater.* 2021;119:104560.
- [28] Migliavacca F, Petrini L, Colombo M, Auricchio F, Pietrabissa R. Mechanical behavior of coronary stents investigated through the finite element method. *J. Biomech.* 2002;35(6):803-11.
- [29] Dolla WJS, Fricke BA, Becker BR. Structural and Drug Diffusion Models of Conventional and Auxetic Drug-Eluting Stents. *J. Med. Devices.* 2006;1(1):47-55.
- [30] Ruan X, Yuan W, Hu Y, Li J, Wu W, Xia R. Chiral constrained stent: Effect of structural design on the mechanical and intravascular stent deployment performances. *Mech. Mater.* 2020;148:103509.
- [31] Ahn BY, Shoji D, Hansen CJ, Hong E, Dunand DC, Lewis JA. Printed Origami Structures. *Adv. Mater.* 2010;22(20):2251-4.

- [32] Kuribayashi K, Tsuchiya K, You Z, Tomus D, Umemoto M, Ito T, et al. Self-deployable origami stent grafts as a biomedical application of Ni-rich TiNi shape memory alloy foil. *Mater. Sci. Eng. A*. 2006;419(1):131-7.
- [33] Javid F, Liu J, Shim J, Weaver JC, Shanian A, Bertoldi K. Mechanics of instability-induced pattern transformations in elastomeric porous cylinders. *J. Mech. Phys. Solids*. 2016;96:1-17.
- [34] Simons MF, Digumarti KM, Conn AT, Rossiter J. Tiled Auxetic Cylinders for Soft Robots. 2019 2nd IEEE International Conference on Soft Robotics (RoboSoft)2019.pp. 62-67.
- [35] Lee JW, Soman P, Park JH, Chen S, Cho D-W. A Tubular Biomaterial Construct Exhibiting a Negative Poisson's Ratio. *Plos One*. 2016;11(5):e0155681.
- [36] Guo Y, Zhang J, Chen L, Du B, Liu H, Chen L, et al. Deformation behaviors and energy absorption of auxetic lattice cylindrical structures under axial crushing load. *Aerosp. Sci. Technol*. 2020;98:105662.
- [37] Zhang XY, Wang XY, Ren X, Xie YM, Wu Y, Zhou YY, et al. A novel type of tubular structure with auxeticity both in radial direction and wall thickness. *Thin-Walled Struct*. 2021;163:107758.
- [38] Wu W, Tao Y, Xia Y, Chen J, Lei H, Sun L, et al. Mechanical properties of hierarchical anti-tetrachiral metastructures. *Extreme Mech. Lett*. 2017;16:18-32.
- [39] Luo C, Han CZ, Zhang XY, Zhang XG, Ren X, Xie YM. Design, manufacturing and applications of auxetic tubular structures: A review. *Thin-Walled Struct*. 2021;163:107682.
- [40] Hedayati R, Güven A, van der Zwaag S. 3D gradient auxetic soft mechanical metamaterials fabricated by additive manufacturing. *Appl. Phys. Lett*. 2021;118(14):141904.
- [41] Ren X, Shen J, Ghaedizadeh A, Tian H, Xie YM. A simple auxetic tubular structure with tuneable mechanical properties. *Smart Mater. Struct*. 2016;25(6):065012.
- [42] Hur JM, Seo D-S, Kim K, Lee JK, Lee KJ, Kim YY, et al. Harnessing distinct deformation modes of auxetic patterns for stiffness design of tubular structures. *Mater. Des*. 2021;198:109376.
- [43] Ansari M, Golzar M, Baghani M, Taghavimehr M, Abbasi Shirsavar M, Yahyavi M. An experimental investigation on shape memory polymer and metallic stents under bending and radial compression. *ERX*. 2020;2(4):045012.
- [44] Wu Z, Zhao J, Wu W, Wang P, Wang B, Li G, et al. Radial Compressive Property and the Proof-of-Concept Study for Realizing Self-expansion of 3D Printing Polylactic Acid Vascular Stents with Negative Poisson's Ratio Structure. *Materials (Basel, Switzerland)*. 2018;11(8).
- [45] ASTM D638-14 Standard test method for tensile properties of plastics. 2014.
- [46] Jiang H, Le Barbenchon L, Bednarczyk BA, Scarpa F, Chen Y. Bioinspired multilayered cellular composites with enhanced energy absorption and shape recovery. *Addit. Manuf*. 2020;36:101430.
- [47] Wong P, Leung Wh, Wong CmJC, diagnosis c. Migration of the AVE Micro coronary stent. 1996;38(3):267-73.
- [48] Pauck RG, Reddy BD. Computational analysis of the radial mechanical performance of PLLA coronary artery stents. *Med. Eng. Phys*. 2015;37(1):7-12.
- [49] Lee SE, Jeong MH, Kim IS, Ko JS, Lee MG, Kang WY, et al. Clinical outcomes and optimal treatment for stent fracture after drug-eluting stent implantation. *J. Cardiol*. 2009;53(3):422-8.
- [50] Jiang H, Zhang Z, Chen Y. 3D printed tubular lattice metamaterials with engineered mechanical performance. *Appl. Phys. Lett*. 2020;117(1):011906.

## Supplementary Information

### S1. Finite element simulation

The setup of finite element simulations for the radial compression of tubular lattice structure is shown in **Fig. S1**. To simulate the experiment of radial compression, two rigid plates were added to the top and bottom to ensure uniform deformation. Reference points were defined to apply the displacement in the simulation. All models in this work were meshed with 3D hexahedral element (C3D8). The ATL structure was meshed with 185,856 hexahedral elements, and the DTL structure was meshed with 276,804 hexahedral elements. General self-contact with friction coefficient of 0.25 was defined for tangential motion and hard contact for the normal direction.

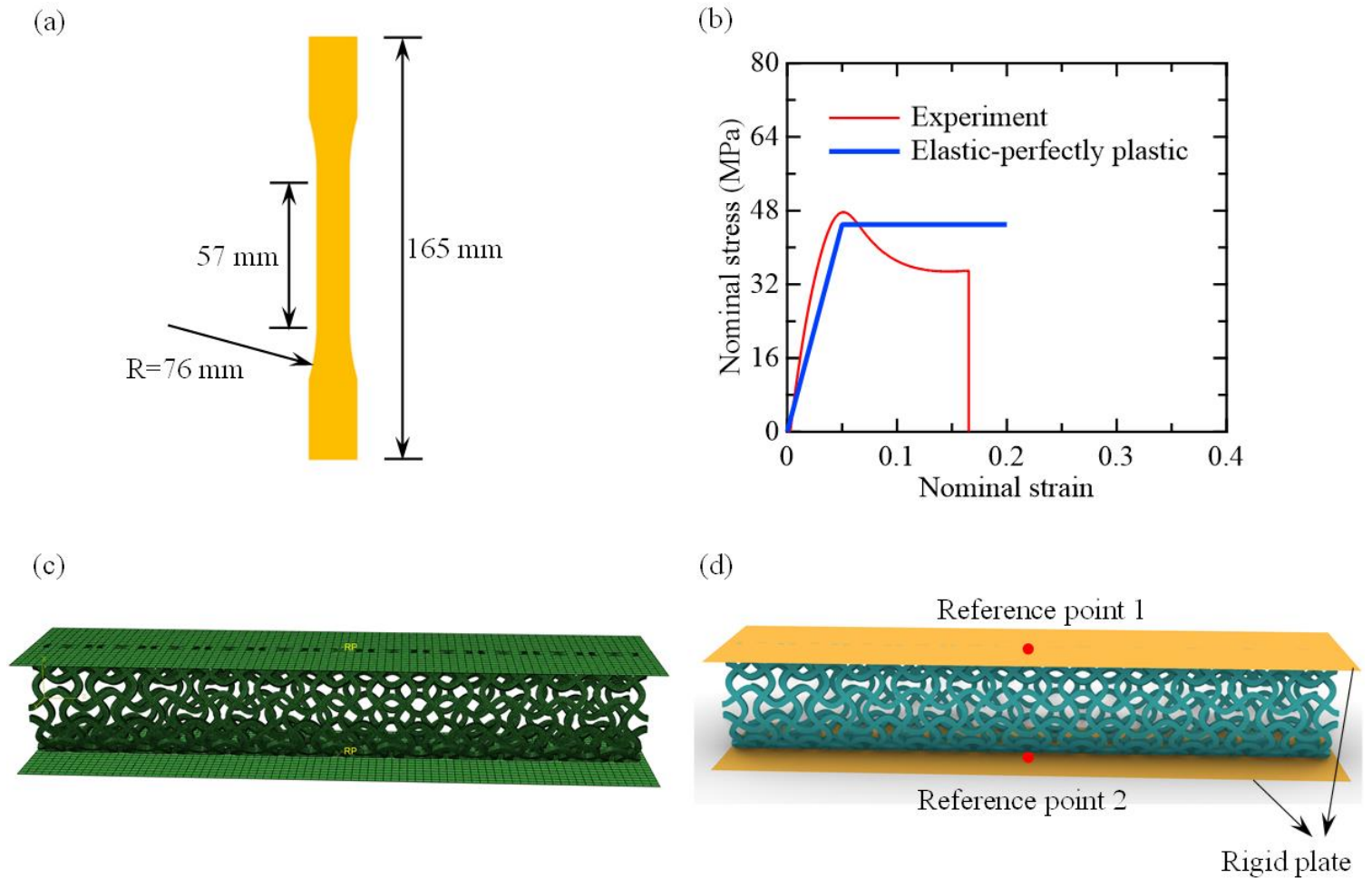


**Fig. S1** Tensile testing and finite element simulation setup. (a) Dumbbell-shape sample. (b) Stress-strain relation of experiment and simplified elastic-perfectly-plastic model. (c) Radial compression setup in Abaqus with rigid plates on the top and bottom. (d) Schematics of the ATL structure with rigid plates and reference points.

## **S2. Comparison of the proposed ATL and the conventional DTL structure**

The detailed comparison of contour plots of stress components is shown in **Figs. S2 (a)-(f)**. We can observe from **Figs. S2 (a)** and **(b)** that the stress component  $\sigma_{xx}$  is more uniformly distributed around the circumferential sinusoidal ligaments, while the straight beams of DTL design are featured by stress concentration of component  $\sigma_{xx}$  on the local joints. The stress component  $\sigma_{yy}$  for ATL is largely spread around the circumferential ligaments near the top and bottom region. However, the stress component is concentrated on the joints of straight beams for DTL near the top and bottom plates. On the other hand, stress component  $\sigma_{zz}$  spreads much more on the axial sinusoidal ligaments than the circumferential ones. Meanwhile, the magnitude of  $\sigma_{zz}$  is smaller than stress component  $\sigma_{xx}$  and  $\sigma_{yy}$ . In addition, the contour plot of displacement along axial direction, as shown in **Figs. S2 (g)** and **(h)**, reveals the effect of auxetic behavior, which shows that the sinusoidal ligaments flow toward the inside of the ATL structure, while the straight beams flow outside of the DTL structure. This unique feature leads to the bending of circumferential sinusoidal ligaments along both radial and axial directions. However, the straight ligaments of DTL structure bend mainly along the radial direction.

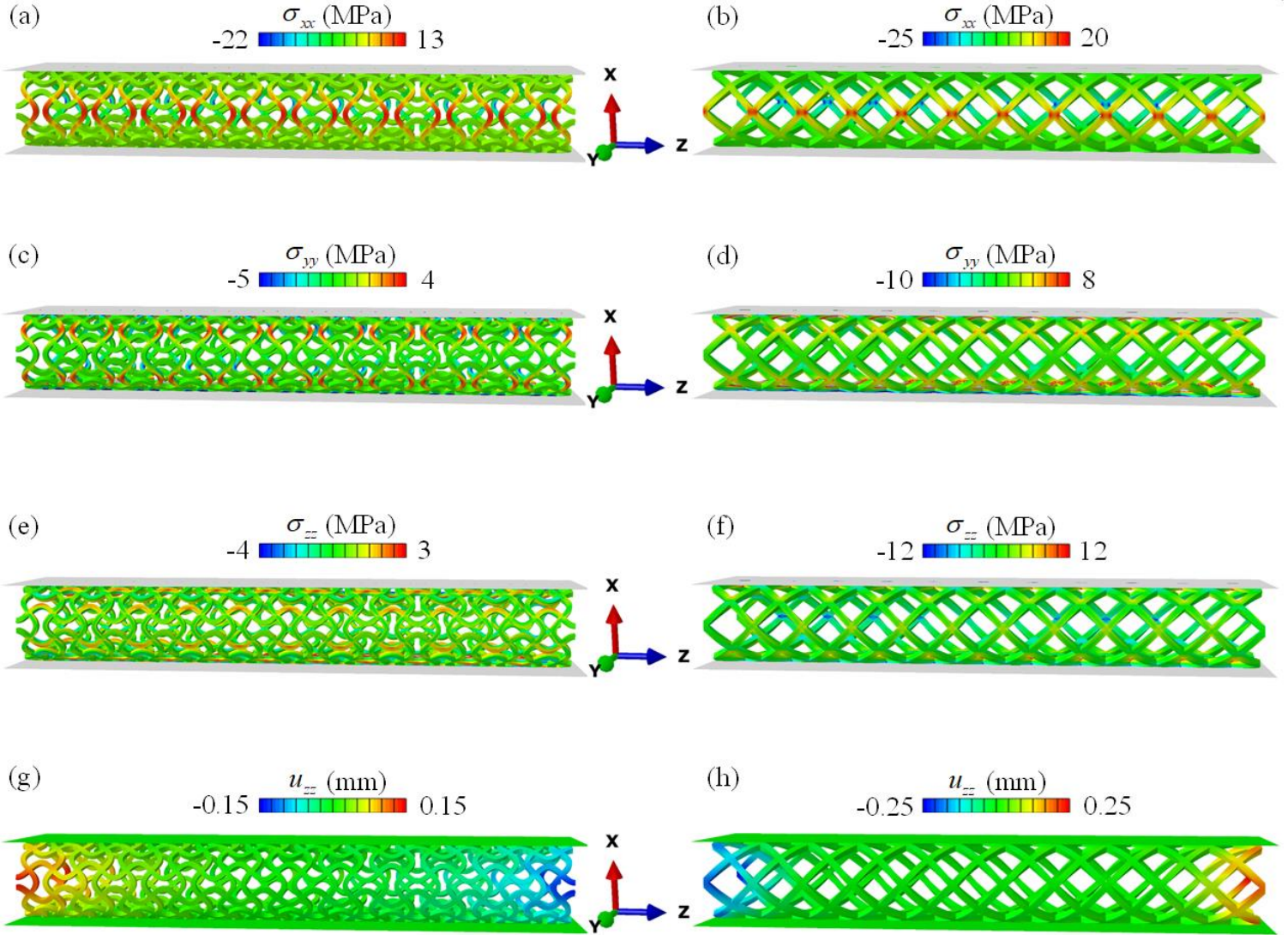


**Fig. S2.** Contour plots of stress components and displacement components under radial compression.

### S3. Effect of beam amplitude

To gain insights from a simulation point of view, we show the contour plots of Mises stress for different beam amplitudes in **Fig. S3**. The contour plots were exported from Abaqus using the same legend. With the increase of beam amplitude, the stress distribution exhibits more uniform pattern. Specifically, when  $A/l = 0.10$ , the stress is slightly more concentrated on the middle part of the circumferential ligaments. As the beam amplitude enlarges, the local stress concentration regions dissipate. As discussed in the main text, this contributes to the increasingly auxetic

effect when  $A/l$  augments. If the beam amplitude is small, the circumferential ligaments bend mainly along radial direction. However, if the beam amplitude is large, the auxetic effect will compel the circumferential ligaments to bend along axial direction as well.

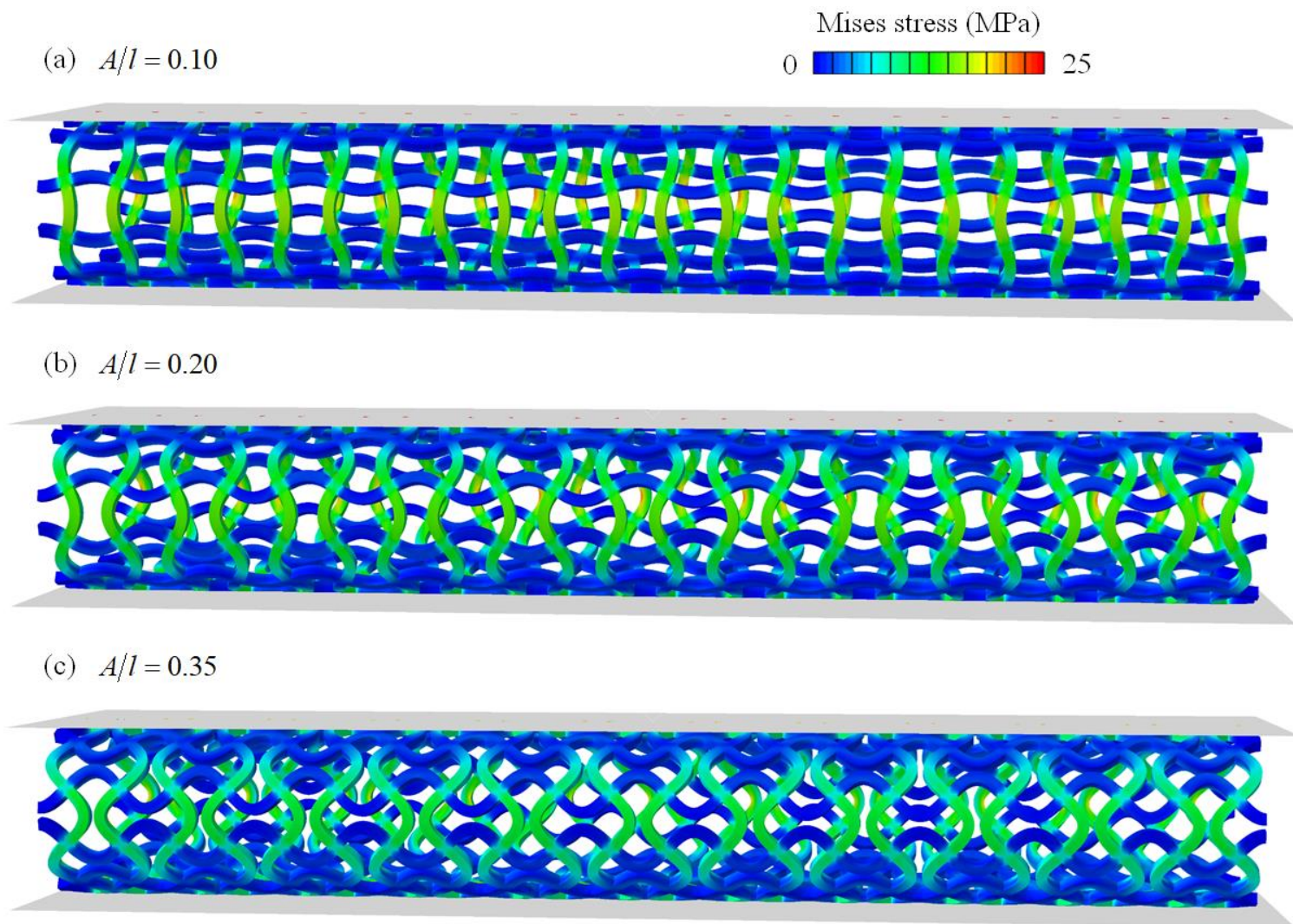


**Fig. S3.** Mises stress contour plots for different beam amplitudes.

## 3D printed tubular lattice metamaterials for mechanically robust stents

Huan Jiang<sup>1</sup>, Hannah Ziegler<sup>1</sup>, Zhennan Zhang<sup>1</sup>, Heng Zhang<sup>2,3</sup>, Louise Le Barbenchon<sup>4</sup>, Sundar Atre<sup>1</sup>, and

Yanyu Chen<sup>1\*</sup>

<sup>1</sup> Department of Mechanical Engineering, University of Louisville, Louisville, KY 40292, USA

<sup>2</sup> Department of Applied Mechanics and Aerospace Engineering, Waseda University, 3-4-1 Okubo, Shinjuku-ku, Tokyo 169-8555, Japan

<sup>3</sup> School of Mechanical Engineering, University of Shanghai for Science and Technology, Shanghai 200093, China

<sup>4</sup> Arts et Métiers ParisTech, CNRS, I2M Bordeaux, Esplanade des Arts et Métiers, Talence Cedex, F-33405, France

\*Corresponding author: Yanyu Chen (yanyu.chen@louisville.edu)

**Abstract:** Coronary artery disease (CAD) is the narrowing or blockage of the coronary arteries, usually caused by atherosclerosis. An interventional procedure using stents is a promising approach for treating CAD because stents can effectively open narrowed coronary arteries to improve blood flow to the heart. However, stents often suffer from catastrophic failures, such as fractures and migration of ligaments, resulting in fatal clinical events. In this work, we report a new type of tubular lattice metamaterial with enhanced mechanical resilience under radial compression, which can be used as an alternative for the current stent design. We begin by comparing the radial mechanical performance of the proposed auxetic tubular lattice (ATL) with the conventional diamond tubular lattice (DTL). Our results show that the ductility of ATL increases by 72.7% compared with that of the DTL structure. The finite element simulations reveal that the stress is more uniformly spread on the sinusoidal ligaments for ATL, while rather concentrated on the joints of straight ligaments for DTL. This phenomenon is intrinsically due to the bending of sinusoidal ligaments along both radial and axial directions, while straight beams bend mainly along the radial direction. We then investigated the effects of the geometrical parameters of the sinusoidal ligament on radial mechanical performance. Experimental results indicate that the beam depth  $h/l$  has the most significant effect on the stiffness and peak load. The stiffness

and maximum load surge by 789% and 1131%, respectively, when  $h/l$  increases from 0.15 to 0.30. In contrast, the beam amplitude  $A/l$  has a minor effect on the stiffness and peak load compared to beam depth and beam thickness. However, increasing the amplitude of the sinusoidal ligament can enlarge the ductility strikingly. The ductility can increase by 67.5% if the amplitude is augmented from  $A/l=0.1$  to  $A/l=0.35$ . The findings from this work can provide guidance for designing more mechanically robust stents for medical engineering.

**Keywords:** tubular structure; stents, metamaterials; ductility; 3D printing

## 1. Introduction

Heart disease is the leading cause of death in many developed countries, with coronary artery disease being the most common form of heart disease. Coronary artery disease (CAD) occurs when excess plaque accumulates in the cardiovascular arteries, resulting in narrowed arteries and restricted blood flow [1-3]. Cardiovascular stents are a non-surgical alternative to traditional treatment options and have become the most common interventional treatment for CAD [4, 5]. Stents are tubular structures that are implanted into obstructed arteries to expand the vessel and prevent arterial collapse. To be successful in clinical use, stents require high stretchability, bending flexibility, and radial strength [6]. Bending flexibility is vital for navigating stent placement and maintaining proper conformability while implanted [7, 8]. However, many conventional stents use straight ligaments, which restrict flexibility during deployment [9]. High radial strength is necessary for maintaining expansion in blocked arteries. Insufficient radial strength and bending flexibility in current stent designs have resulted in failure events such as stent collapse and migration [10-13]. Catastrophic failure of stent geometry also creates a risk of vessel perforation.

To overcome the limitations of existing stent designs, improvements to stent bending flexibility and radial strength have been explored. Stent radial strength is largely related to the mechanical properties of the base material and stent strut geometry [14]. As such, many studies have explored stent materials different from the original nitinol [15]. For example, composite metal-polymer braided stents have shown improved radial strength over braided nitinol

stents [16]. Thin membranes on the inner and outer surface of tubular structures have also been shown to increase the radial stiffness of traditional stent designs [17, 18]. More recently, biodegradable stent materials have been investigated for improved stent biocompatibility and bending flexibility, despite reduced radial strength compared to metal stents [19, 20]. Additionally, studies have explored the effects of changing geometric parameters on existing stent architectures. García et al. demonstrated control of stent radial stiffness through varied strut thickness and used these findings to develop a stent for variable radial force [21]. Strut geometry and connection type have also been used to vary stent bending flexibility [7, 20, 22]. In contrast to these commonly adopted methods, this research aims to develop new architectures to improve the radial behavior of tubular structures under large deformation.

Stent geometry has previously been limited by constraints of top-down fabrication methods. Due to the growing prevalence of additive manufacturing techniques, more complex tubular structures have been developed in recent years to address stent limitations [23-30]. For example, origami-inspired tubular structures have been studied for their improved producibility and versatility [31]. Foldable origami stents achieved favorable radial compressive strength using a single material, compared to dual material covered stents which risk incompatibility between stent and graft [32]. Tubular lattice structures have also been explored for their unique mechanical performance. For instance, the observed buckling response of cylindrical shell tubular lattices was highly non-linear and could be controlled through unit cell geometry [33]. Additionally, tubular auxetic materials have recently gained popularity for their novel behavior and tunable mechanical properties [34-39]. Auxetic materials exhibit a negative Poisson's ratio, which provides superior conformability during stent operation. Select microstructures exhibit auxetic behavior in compression, but not in tension, for wrinkle-free bending [40]. Controllable buckling response, bending flexibility, and torsional stiffness have also been investigated in tubular auxetics [23, 33, 40-42]. Mechanical performance of auxetics can be adjusted by modifying unit cell geometric parameters and base material, enabling stent customization.

There are very few studies focused on the radial compression behavior of tubular auxetics. Metallic Omega stent with helical connector design topology was investigated under radial compression and compared with shape memory

polymeric stent at different temperature scenarios [43]. It is reported that the radial strength hardly varies at the body temperature range and the metallic Omega stent shows higher radial force, indicating the effectiveness of supporting the arterial walls of vessel for the metallic Omega stent. However, this study is focused on the comparison of radial compression behavior for different materials, instead of considering the effect of the topology of stent. An auxetic vascular stent with arrowhead design was explored for the radial compression performance [44]. It is found that the increase of the wall thickness raises the ability of stent to resist radial deformation and the enlargement of stent diameter decreases the radial strength. However, their study did not explain how the auxetic effect contributes to the radial compression behavior.

In this work, we present a novel tubular lattice structure with auxetic unit cells for improved radial performance under large compressive deformation, and the mechanical response of the auxetic design was compared to a traditional, Palmaz-Schatz inspired, diamond lattice design [9] through a combined experimental and numerical approaches. Specifically, the finite element analyses (FEA) were conducted to provide additional insights for the mechanisms in the compressive deformation. As a novel contribution of this work, we proposed a newly designed Auxetic Tubular Lattice (ATL) structure and studied the effects of tubular lattice topology and the geometric parameters on the radial compression performance. In addition, we explained the auxetic effect on the radial compression behavior from numerical findings. Our experimental and numerical studies reveal the robust mechanical performance of the ATL structure.

## 2. Material and Methods

### 2.1 Tubular lattice metamaterials design

The design procedure of the proposed tubular metamaterial, namely auxetic tubular lattice (ATL), is illustrated in **Figs.1 (a)-(c)**. The 2D auxetic unit cell can be described by the parameters  $l$ ,  $t$  and  $A$ , where  $2l$  is the lattice constant of the unit cell,  $t$  is the thickness and  $A$  denotes the amplitude of the sinusoidal ligament. The 3D Representative Volume Element (RVE) consists of six bent 2D unit cells along the circumferential direction and one unit cell along

the axial direction. In the RVE,  $2l$  denotes the height,  $D$  represents the diameter of the circle,  $t$  and  $h$  denote the thickness and depth of the sinusoidal ligament, respectively. The 3D ATL model contains 11 RVEs along the axial direction. A 3D printed ATL is shown in **Fig. 1 (d)**. For comparison, we also designed a conventional tubular lattice as a benchmark, namely diamond tubular lattice (DTL). This structure is assembled using the same procedure, as shown in **Figs. 1 (e)-(g)**. DTL structure shares the same lattice constant  $2l$  and circle diameter  $D$  as ATL structure. To ensure the two configurations have the same mass, the thickness and depth of the beam are represented by different parameters  $p$  and  $q$ . A 3D printed DTL structure is shown in **Fig. 1 (h)**.

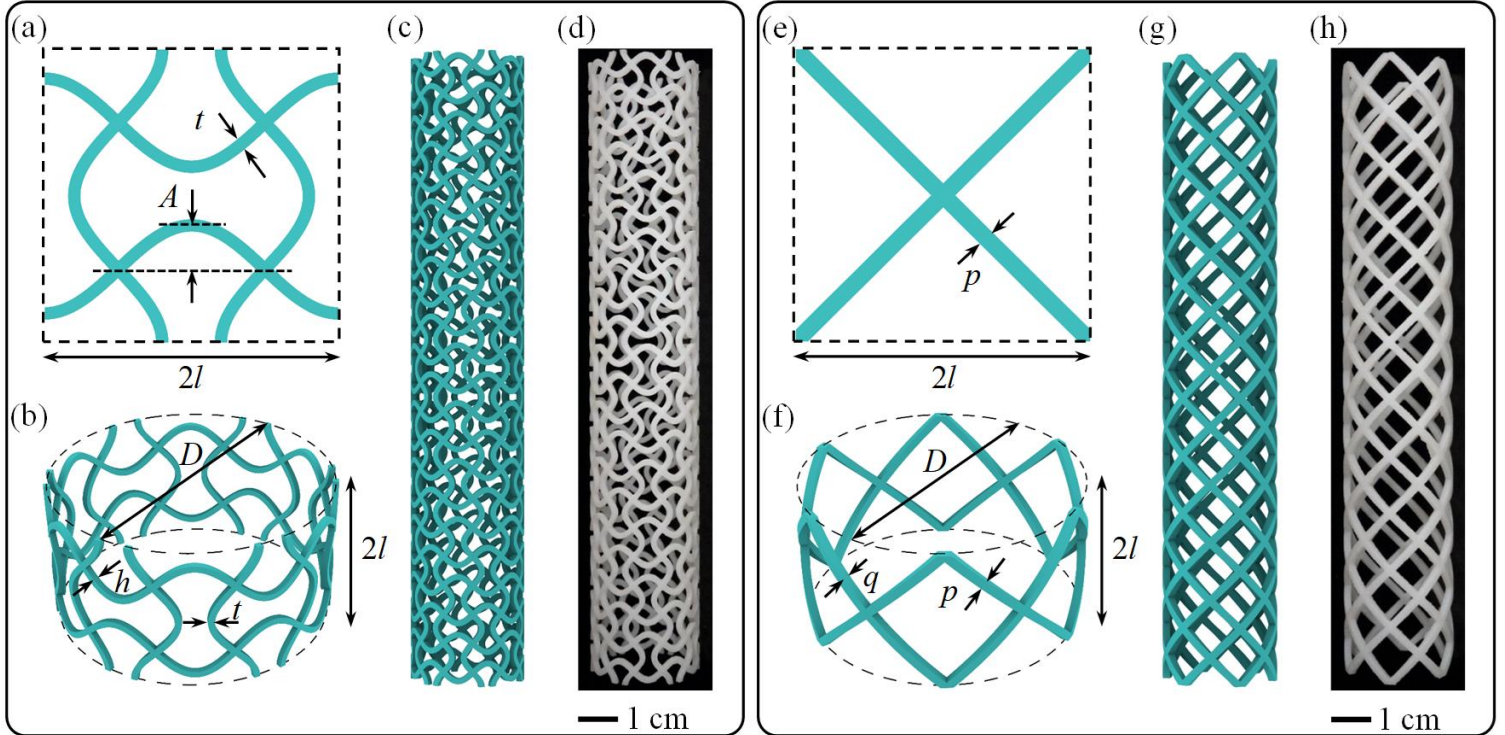


**Fig. 1.** Auxetic tubular lattice (ATL) and diamond tubular lattice (DTL) design. (a) 2D unit cell design of ATL.  $2l$  is the lattice constant of the unit cell,  $t$  is the thickness and  $A$  denotes the amplitude of sinusoidal ligament. (b) 3D Representative Volume Element (RVE) with six bent unit cells along the circumferential direction and one unit cell along the axial direction. Here,  $2l$  denotes the height of the RVE,  $D$  represents the diameter of the circle,  $t$  and  $h$  denote the thickness and depth of the sinusoidal ligament, respectively. (c) Geometrical model of ATL, with 11 RVEs

along the axial direction. (d) 3D printed sample of ATL. Here  $l = 7$  mm,  $D = 84/\pi$ ,  $A/l = 0.3$ ,  $t/l = 0.2$ ,  $h/l = 0.2$ . (e) 2D unit cell design of DTL.  $2l$  is the lattice constant of the unit cell,  $p$  is the thickness of the straight ligament. (f) 3D RVE with six unit cells along the circumferential direction and one unit cell along the axial direction. Here,  $2l$  denotes the height of the RVE,  $D$  is the diameter of the circle,  $p$  and  $q$  represent the thickness and depth of the beam, respectively. (g) Geometrical model of DTL, with 11 RVEs along the axial direction. (h) 3D printed sample of DTL. Here  $l = 7$  mm,  $D = 84/\pi$ ,  $p = q = 1.828$  mm.

## 2.2 Tubular lattice metamaterials fabrication

Polyjet additive manufacturing of photocurable resins is employed to fabricate the ATL and DTL structures. This technique enables the fabrication of complex structures with spatially varying geometry. CAD models of the tubular lattice structures were created using Rhinoceros® add-on Grasshopper (Robert McNeel & Associates, Seattle, USA). In this study, Object260 Connex Polyjet 3D printer (Stratasys Ltd., USA) is used for sample fabrication. This 3D printer employs polymer jetting technology which uses small nozzles to dispense liquid photopolymerizable monomer from a print head, which is then immediately cured by ultraviolet (UV) light using a source situated on-board of the printing head. With this printer, samples can be fabricated with a resolution of 16  $\mu\text{m}$  in the z-direction and 42  $\mu\text{m}$  in the x- and y-directions. Herein, a rigid polymer material, VeroWhitePlus, 1 is used to fabricate all the samples in a layer-by-layer fashion. A support material, SUP706, is used to improve the surface finish of the samples and to provide support for overhanging structures and can be removed by water jetting.

## 2.3 Radial compression testing

Quasi-static compression tests on ATL and DTL structures along radial direction are conducted using the Instron 5569A–Universal testing machine with a load cell of 50 kN. All samples are tested in displacement control mode at 3 mm/min with a final compression depth of 18 mm. The mechanical performance of the 3D printed specimens is first investigated by considering two geometric configurations (ATL and DTL). Then, the effects of beam depth  $h$ ,

thickness  $t$ , and amplitude  $A$  for ATL metamaterial are individually studied. An ARAMIS 4 M system (GOM GmbH, Germany) is used to capture deformations. Repeated testing is performed to ensure the reliability of the data. The effective stiffness, maximum load, and ductility are extracted from the measured load-displacement curve for each test.

## 2.4 Finite element simulation

Finite element simulations are conducted to provide additional insights into the compressive deformation mechanisms of the tubular lattice structures. The commercial software Abaqus/explicit (Providence, RI, USA) is employed for the simulations. The elastic-perfectly-plastic constitutive model is adopted to simulate the VeroWhitePlus polymer. Tensile testing is performed per the ASTM standard [45] to obtain the material properties. The dumbbell-shape sample is shown in **Fig. S1 (a)**, and the simplified constitutive model is shown in **Fig. S1 (b)**. From the experimental data, we choose Young's modulus  $E = 1000$  MPa and yield strength is set to  $\sigma_y = 45$  MPa. Poisson's ratio  $\nu = 0.33$  is chosen from reference [46]. All tubular lattice structures are meshed with  $\sim 200,000$  C3D8 elements by using Hypermesh (Altair Engineering Inc., USA). The detailed finite element simulation setup is shown in **Fig. S1 (c)** and **(d)**. The convergence test is performed to eliminate the effect of mesh size. Meanwhile, the ratio of kinetic energy to the internal energy is controlled below 5% to get rid of the dynamic effect.

## 3. Results and discussion

### 3.1 Comparison between the proposed design and conventional design

To compare the proposed design and conventional design under compressive load, we performed compression tests on ATL and DTL samples. Each design was tested three times to eliminate the possibility of rare types of error that may be involved in these experiments. **Fig. 2 (a)** shows the load-displacement curves of ATL and DTL designs. Compared to the catastrophic failure of the DTL structure, the ATL exhibits a progressive failure mode. For the DTL structure, the load dropped significantly at a displacement of 4.8 mm, i.e., 88% loss of load. However, the ATL

structure showed no serious load drop during the process of compression, indicating a more ductile behavior. **Fig. 2 (b)** displays the comparison of stiffness, maximum load, and ductility of ATL and DTL designs. The ductility in this work was defined as the ratio of displacement at a 25% drop from the peak load to the maximum displacement, i.e., 18 mm. The error bars from repeated testing in **Fig. 2 (b)** show that the experiments repeated very well. Both stiffness and maximum load of ATL structure are smaller than that of DTL structure. However, the ductility of ATL increases by 72.7% compared to the DTL design.

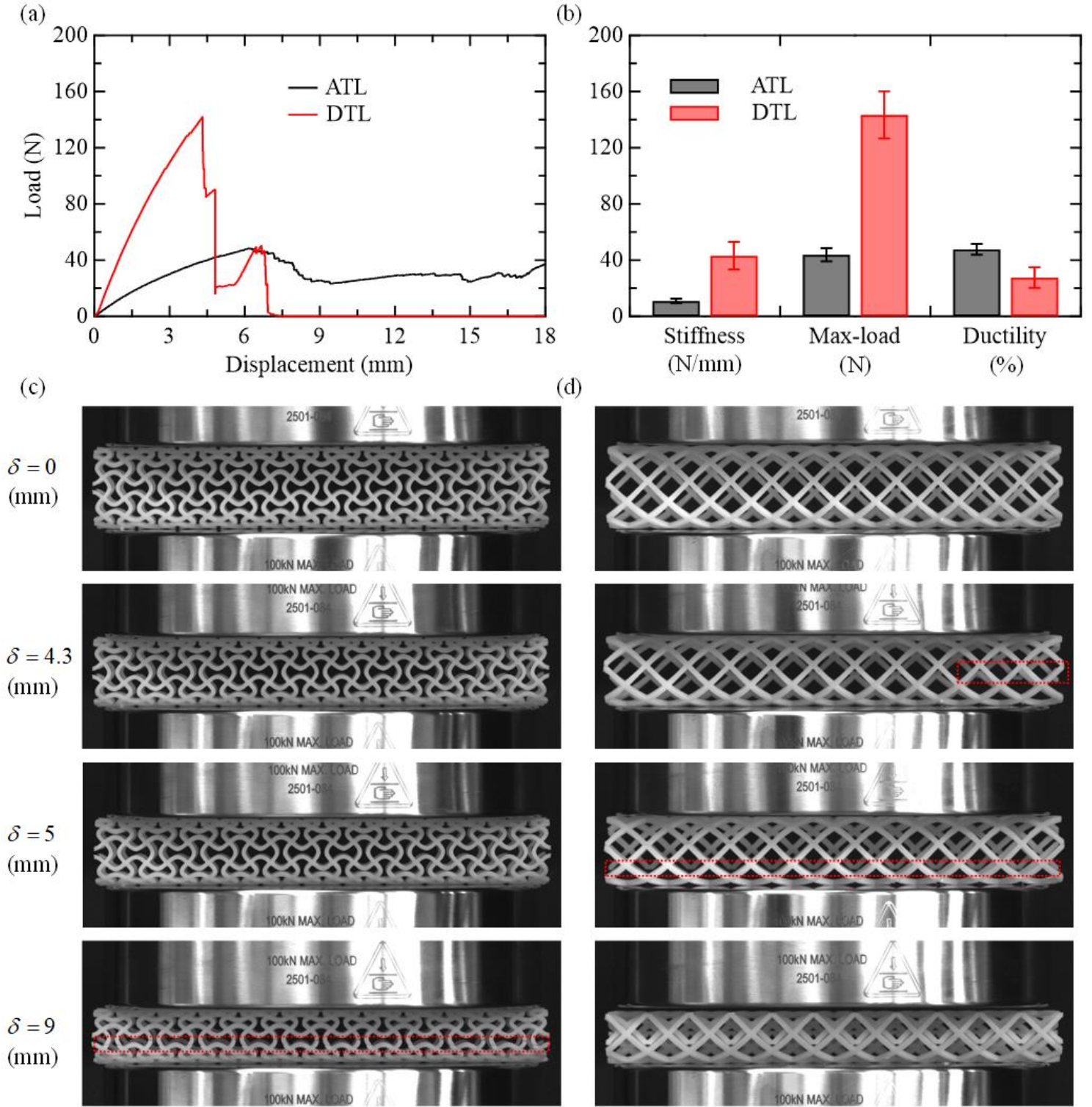


**Fig. 2.** Mechanical performance of ATL and DTL structures under compression. (a) Load-displacement curves for ATL and DTL. (b) Comparison of stiffness, maximum load, and ductility of ATL and DTL. (c) Deformation patterns

for ATL. Here,  $l = 7$  mm,  $D = 84/\pi$ ,  $A/l = 0.3$ ,  $t/l = 0.2$ ,  $h/l = 0.2$ . (d) Deformation patterns for DTL. Here,  $l = 7$  mm,  $R = 84/\pi$ ,  $p = q = 1.828$  mm.

**Figs. 2 (c)-(d)** display the deformation evolutions of ATL and DTL structures under different displacements. At the displacement of  $\delta = 4.3$  mm, the ATL design shows no observable failure. However, the DTL design breaks at the joints of straight beams, as highlighted in the image. This failure corresponds to the load drop in the load-displacement curve. At the displacement of  $\delta = 5$  mm, ATL structure still shows no observable failure, while DTL design exhibits complete dislocation at the joints, highlighted in the image across the sample. This contributes to the further load drop of 88% in the load-displacement curve. As the displacement rises to  $\delta = 9$  mm, fractures are generated in the ATL structure, shown in the highlighted region. However, the integrity of the ATL structure is not affected despite these fractures, indicating a remarkably ductile performance. On the other hand, the DTL design is characterized by a complete dislocation at multiple joints, leading to the total collapse of the specimen. This explains the plummet of load to zero.

To gain further insights into the mechanisms that are responsible for the disparate deformations of ATL and DTL structures, finite element simulations were performed. The simulated and measured load-displacement curves for ATL and DTL structures are shown in **Figs. 3 (a)** and **(b)**, respectively. The simulations were conducted to reveal the mechanisms before fracture. Therefore, we did not consider the failure in our simulations. **Figs. 3 (c)** and **(d)** show the Mises stress contour plots of ATL and DTL structures under different compressive displacements. One can observe that the Mises stress for the ATL structure is more uniformly distributed on the circumferential ligaments, while the stress for DTL design is rather concentrated on the joints of straight ligaments. It is also interesting to see that the axial sinusoidal ligaments of the ATL structure do not significantly contribute to bearing the load. The detailed distribution of stress components for ATL and DTL design is shown in **Fig. S2** in the Supplementary Information (SI). **Figs. S2 (a)** and **(b)** display the  $\sigma_{xx}$  for the ATL and DTL structures, respectively. It is apparent that the stress component  $\sigma_{xx}$

is largely distributed on the circumferential ligaments in the middle region between the top and bottom plates for ATL design, and mostly concentrated on the joints for the DTL design. The stress component  $\sigma_{yy}$  is widely distributed on the circumferential ligaments close to the top and bottom plates, while mainly concentrated on the joints near the top and bottom plate. On the other hand, the stress component  $\sigma_{zz}$  is primarily spread on the axial ligaments along the sample for ATL. However, the magnitude of  $\sigma_{zz}$  is significantly smaller compared to  $\sigma_{xx}$ . Furthermore, the contour plot of displacement along the axial direction shown in **Figs. S2 (g) and (h)** reveals an auxetic effect, which shows that the sinusoidal ligaments flow toward the inside of the ATL structure, while the straight beams flow toward the outside of the DTL structure. This unique feature leads to the bending of circumferential sinusoidal ligaments along both radial and axial directions. However, the straight ligaments of the DTL structure bend along the radial direction.

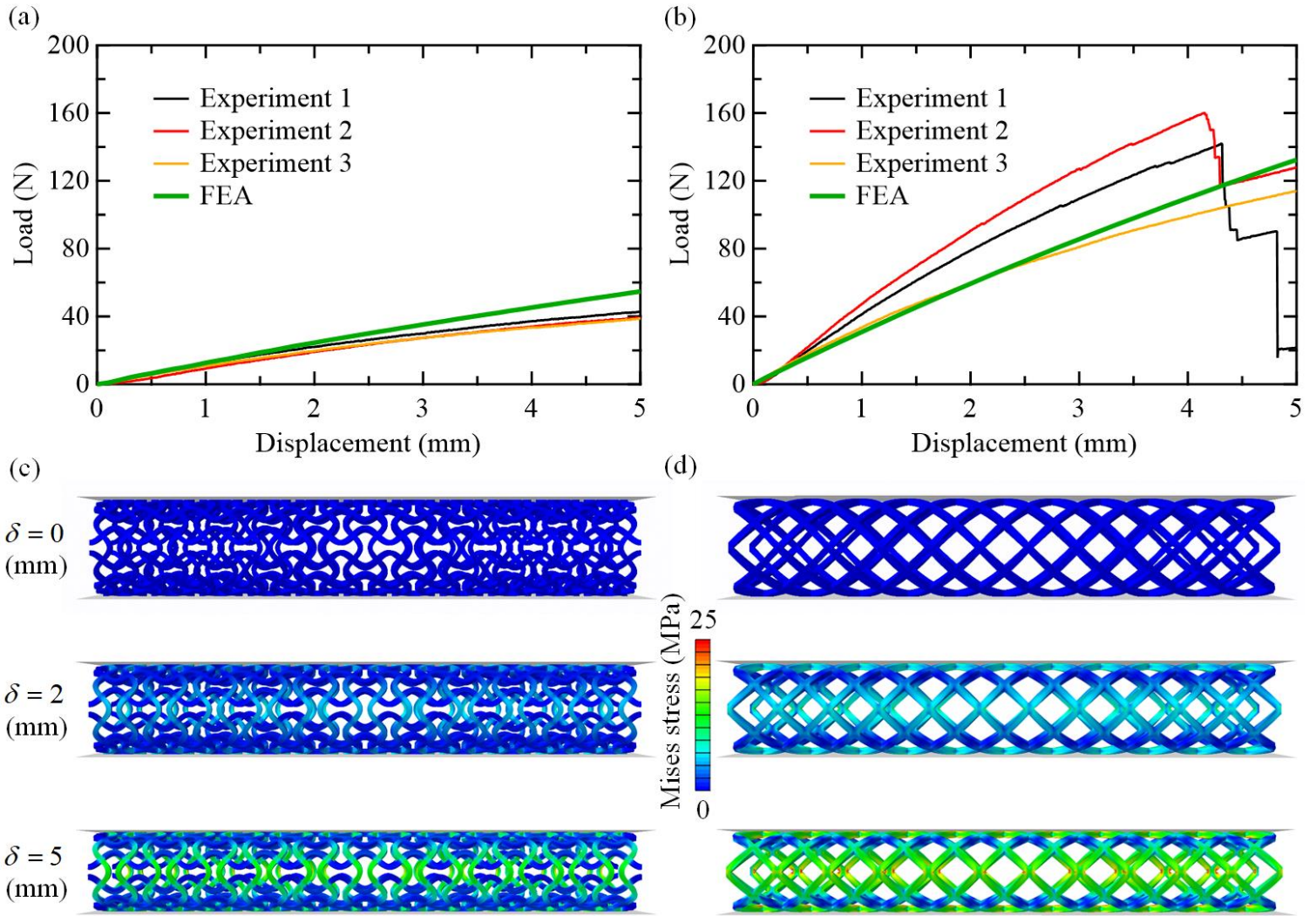


**Fig. 3.** Finite element simulations for ATL and DTL structures. (a) Measured and simulated load-displacement curves for ATL structure. (b) Measured and simulated load-displacement curves for DTL structure. (c) Mises stress contour plots for ATL. (d) Mises stress contour plots for DTL.

For vascular stents, radial strength is a primary design requirement to withstand compressive forces exerted by the vascular wall. On the one hand, insufficient radial strength during the revascularization and early stage of restoration causes acute elastic recoil of the artery and frequent migration [47, 48]. On the other hand, the catastrophic failure of stent could induce protrusion into the vessel lumen and trigger platelet activation [49], which poses serious threat to patients. Therefore, the stent with sufficient radial strength and the capacity to prevent catastrophic failure

are required as the ideal candidate for clinical usage. In the above investigation, we demonstrate that although the DTL structure displays higher radial strength than that of the ATL architecture, it suffers from disastrous collapse once the radial strength is reached. The ATL design shows more ductility than the DTL one, which indicates the small amount of radial strength drop after the peak point. Note that the overall radial strength of ATL is comparatively smaller than DTL. To demonstrate the advantage of ATL design, we will show the tunability of radial strength for ATL design without sacrificing its ductility by performing parametric analyses.

### 3.2 Effect of beam depth

Having studied the mechanical performance of the proposed tubular lattice architecture, we proceed to demonstrate the design flexibility of ATL design by altering the geometric parameters of the sinusoidal ligament, including beam depth  $h$ , beam thickness  $t$ , and beam amplitude  $A$ . We start by investigating the effect of beam depth  $h/l$  on mechanical performance. The shape evolution for different beam depths is shown in **Fig. 4 (a)**. The measured load-displacement relations for different beam depths are displayed in **Fig. 4 (b)**. One can observe that the load drop is increasingly significant with the enlargement of beam depth, indicating a more brittle failure mode for large beam depth. As summarized in **Figs. 4 (c) and (d)**, both the stiffness and maximum load show an increasing trend with the augment of beam depth. Particularly, the stiffness and maximum load surge by 789% and 1131%, respectively, when  $h/l$  increases from 0.15 to 0.30. **Fig. 4 (e)** displays the ductility of the ATL structure with various beam depths. The ductility for different beam depth models remains relatively high, i.e., ~40%, compared with what we reported for DTL design.

**Figs. 5 (a) and (b)** display the deformation patterns for ATL design with  $h/l = 0.15$  and  $h/l = 0.30$ , respectively. For the convenience of description, we will use the model parameter to represent the model throughout the work. For instance, we use  $h/l = 0.15$  to denote the ATL structure with  $h/l = 0.15$ . At the displacement of  $\delta = 7.1$  mm,  $h/l = 0.15$  shows fractures in the middle region, as highlighted in the image. The  $h/l = 0.30$ , on the other hand, exhibits

fewer fractures in the highlighted area at this stage. However, the load drop for  $h/l = 0.30$  is more rapid than that of  $h/l = 0.15$  as seen from the load-displacement curves in **Fig. 4 (b)**, indicating the catastrophic failure of  $h/l = 0.30$ . At the displacement of  $\delta = 10$  mm,  $h/l = 0.15$  shows a similar fracture pattern to the previous stage, and the sample maintains the integrity of the structure. In contrast, disastrous failure occurs at this point for  $h/l = 0.30$ , as can be observed from the image where the highlighted part breaks off from the sample. This observation verifies our previous description of catastrophic failure for  $h/l = 0.30$ .

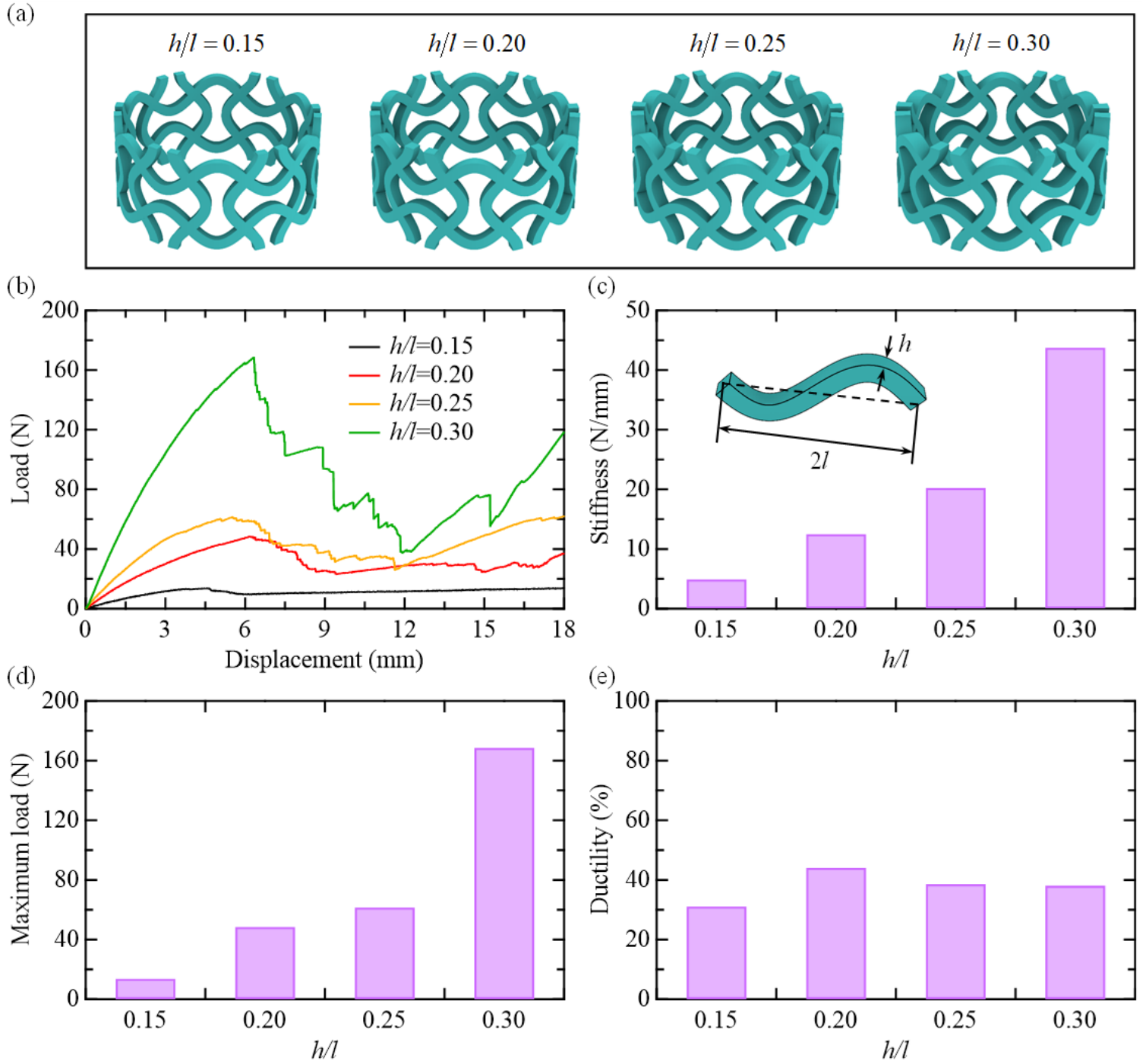


**Fig. 4.** Effect of beam depth on the performance of ATL structure. (a) RVEs with different beam depths. (b) Load-displacement curves. (c) Tubular lattice stiffness as a function of  $h/l$ . (d) Tubular lattice maximum load as a function of  $h/l$ . (e) Tubular lattice ductility as a function of  $h/l$ . Here,  $l = 7$  mm,  $D = 84/\pi$ ,  $A/l = 0.3$ ,  $t/l = 0.2$ .

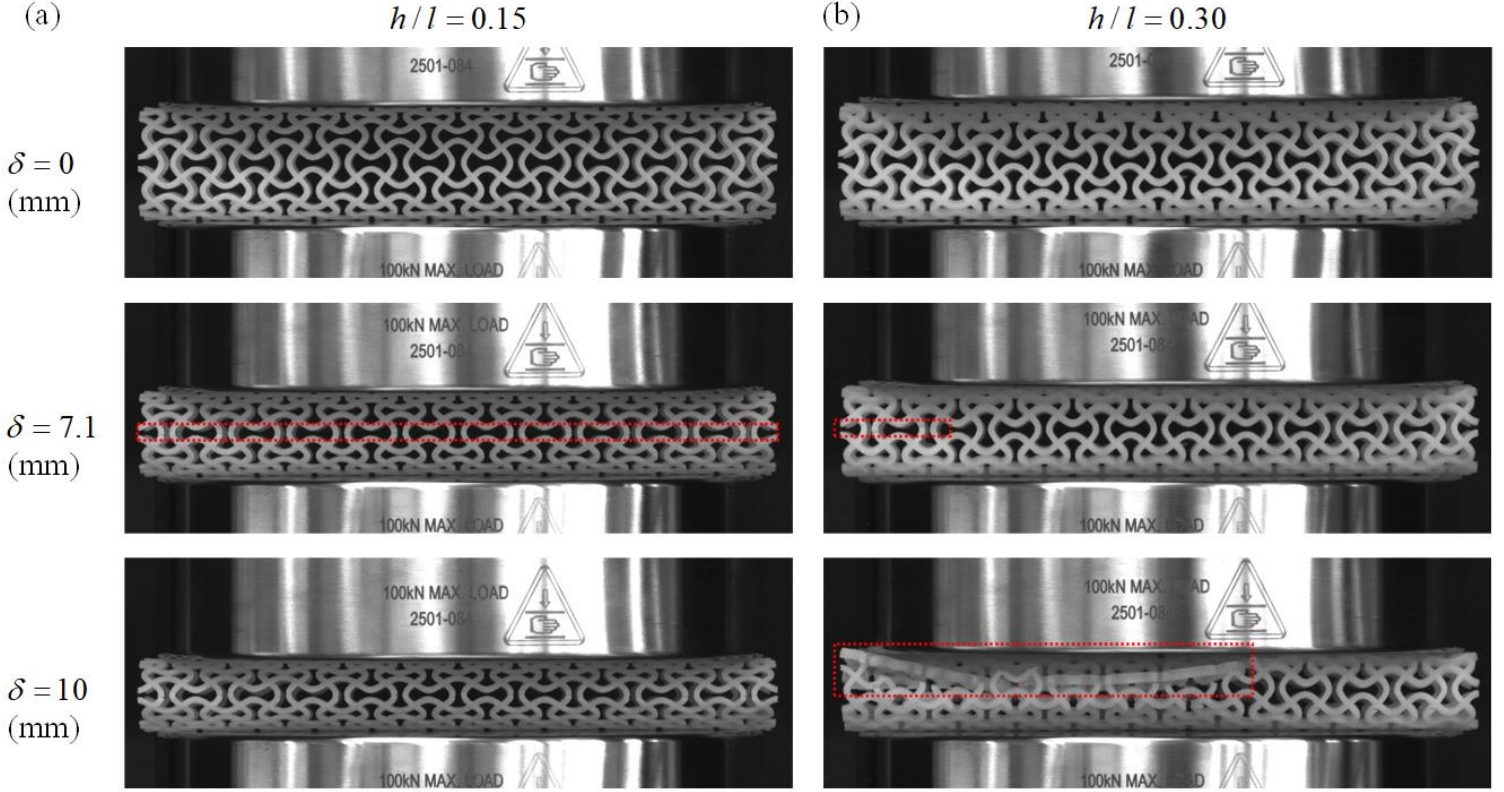


**Fig. 5.** Comparison of deformation patterns for ATL structure with different beam depths. (a) Deformation patterns for  $h/l = 0.15$ . (b) Deformation patterns for  $h/l = 0.30$ .

### 3.3 Effect of beam thickness

In this section, we proceed to investigate the effect of beam thickness  $t$  on the mechanical performance of the ATL structure. RVEs with different beam thicknesses are schematically shown in **Fig. 6 (a)**. The load-displacement curves for different beam thicknesses are shown in **Fig. 6 (b)**. One can observe that the ATL structure tends to exhibit a more brittle failure phenomenon with the increase of beam thickness  $t$ , similar to the effect of beam depth  $h$ . **Figs. 6 (c) and (d)** display stiffness and maximum load for various beam thickness models. The stiffness and maximum load are enhanced by 241% and 231%, respectively, when the beam thickness enlarges from  $t/l = 0.15$  to  $t/l = 0.30$ . This indicates that the contribution of beam thickness is significantly smaller compared to that of beam depth. This phenomenon can be intrinsically explained by analogy to beam theory. For the compression case in our work, the

bending stiffness of the sinusoidal ligaments can be expressed by  $M = CE\kappa th^3$  [50]. Here,  $C$  is the geometric constant,  $E$  is Young's modulus, and  $\kappa$  is the curvature. Therefore, beam depth  $h$  has a more important role than beam thickness  $t$  in this scenario. **Fig. 6 (e)** shows the ductility of ATL design with different beam thicknesses. Ductility for all the studied samples was relatively high, i.e., ~40%, indicating a superior compliant behavior compared to the DTL structure.

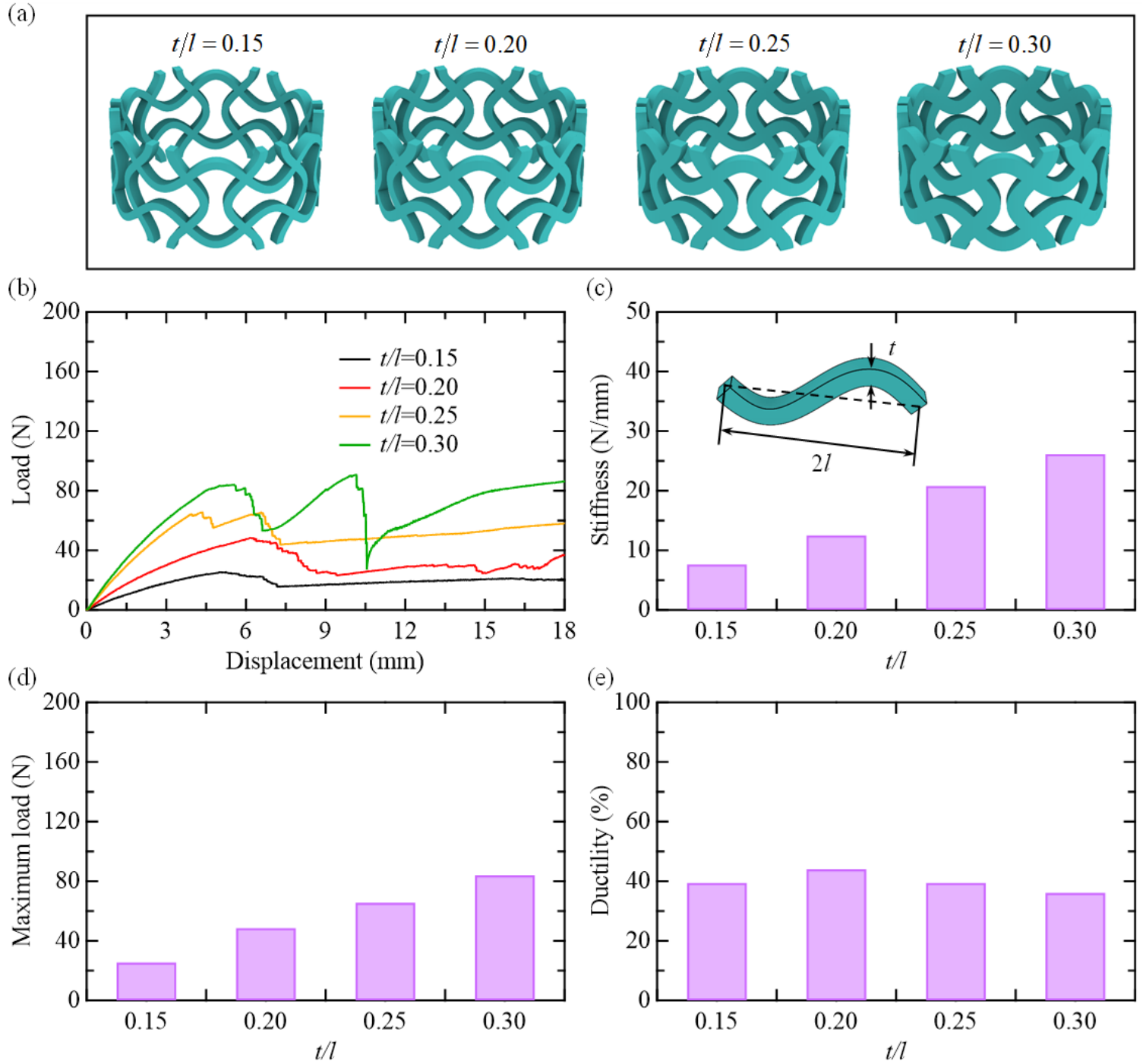


**Fig. 6.** Effect of beam thickness on the performance of ATL structure. (a) RVEs with different beam thicknesses. (b) Load-displacement curves. (c) Tubular lattice stiffness as a function of  $t/l$ . (d) Tubular lattice maximum load as a function of  $t/l$ . (e) Tubular lattice ductility as a function of  $t/l$ . Here,  $l = 7$  mm,  $D = 84/\pi$ ,  $A/l = 0.3$ ,  $h/l = 0.2$ .

**Figs. 7 (a)** and **(b)** show the deformation evolutions for  $t/l=0.15$  and  $t/l=0.30$ , respectively. At the displacement of  $\delta = 7$  mm, we can observe multiple fractures for  $t/l=0.15$  in the region highlighted in the image. A similar fracture pattern happened for  $t/l=0.30$  as well, as shown in the highlighted region. However, the difference is that the load drops due to the ligament failure for  $t/l=0.30$  is much more rapid than that of  $t/l=0.15$ , as seen in the load-displacement relation in **Fig. 6 (b)**. This indicates a more brittle failure for a larger beam thickness model. At the displacement of  $\delta = 10.6$  mm,  $t/l=0.15$  exhibits analogous fracture pattern to the previous stage. On the other hand,  $t/l=0.30$  displays a significantly different failure manner. The symmetry of the model has been completely destroyed, which can be seen by looking at the holes highlighted in the image. Meanwhile, a considerable load plummet occurs at this point. These facts indicate a catastrophic failure of  $t/l=0.30$  at this stage.

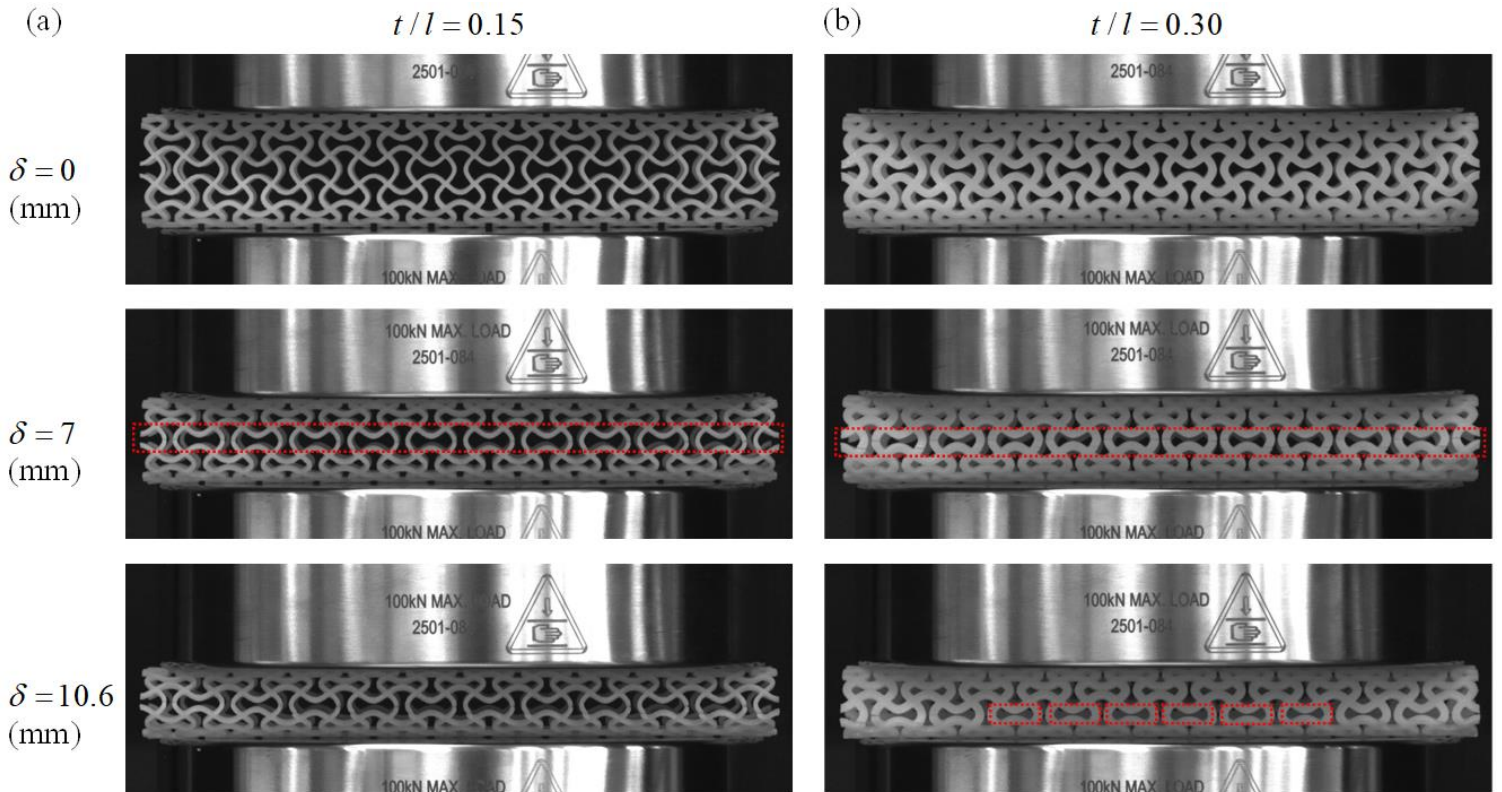


**Fig. 7.** Comparison of deformation patterns for ATL structure with different beam thickness. (a) Deformation patterns for  $t/l = 0.15$ . (b) Deformation patterns for  $t/l = 0.30$ .

### 3.4 Effect of beam amplitude

In this part, we proceed to investigate the effect of beam amplitude on the mechanical performance of the ATL structure. The RVEs with different beam amplitudes are shown in **Fig. 8 (a)**. The load-displacement relation curves for different beam amplitudes are shown in **Fig. 8 (b)**. Stiffness shows a decreasing trend with the increase of the beam amplitude, and the finite element simulation results in the inset verify this finding. Furthermore, the yield load occurs at larger displacement when the beam amplitude becomes bigger, indicating a more compliant behavior. **Figs. 8 (c) and (d)** display the category plot of stiffness and maximum load, respectively. The stiffness exhibits a decreasing trend with increasing amplitude as observed from the load-displacement curves. Particularly, the stiffness is reduced by 61.5% when the amplitude is enlarged from  $A/l = 0.1$  to  $A/l = 0.35$ . On the other hand, the maximum load does not show a pattern due to the randomness of failure. Quite interestingly, the beam amplitude is found to have a less significant effect on the load-displacement response than beam thickness and depth. This is different from what we reported in the tensile testing in our previous work [50]. **Fig. 8 (e)** shows the ductility of ATL design with various beam amplitude. The ductility is discovered to exhibit an increasing trend with the augment of beam amplitude. To further investigate the mechanism behind this phenomenon, we show the contour plot of Mises stress for different beam amplitude models in **Fig. S3**. As one increases the amplitude, a more uniform stress distribution is observed. For  $A/l = 0.10$  in **Fig. S3 (a)**, the stress is slightly concentrated on the middle part of the circumferential ligaments. However, the local concentrated regions dissipate gradually as the beam amplitude enlarges, as shown in **Figs. S3 (b) and (c)**. This attributes to the auxetic effect which we have discussed in section 3.1. The circumferential ligaments bend mainly along the radial direction due to the little auxetic effect when the beam amplitude is small. In contrast, the notable auxetic effect will compel the circumferential ligaments to bend along both radial direction and axial

direction as the beam amplitude increases. Particularly, the ductility is enhanced by 225% if the beam amplitude is enlarged from  $A/l=0.1$  to  $A/l=0.35$ , where the  $A/l=0.35$  displays ductility up to 67.5%.

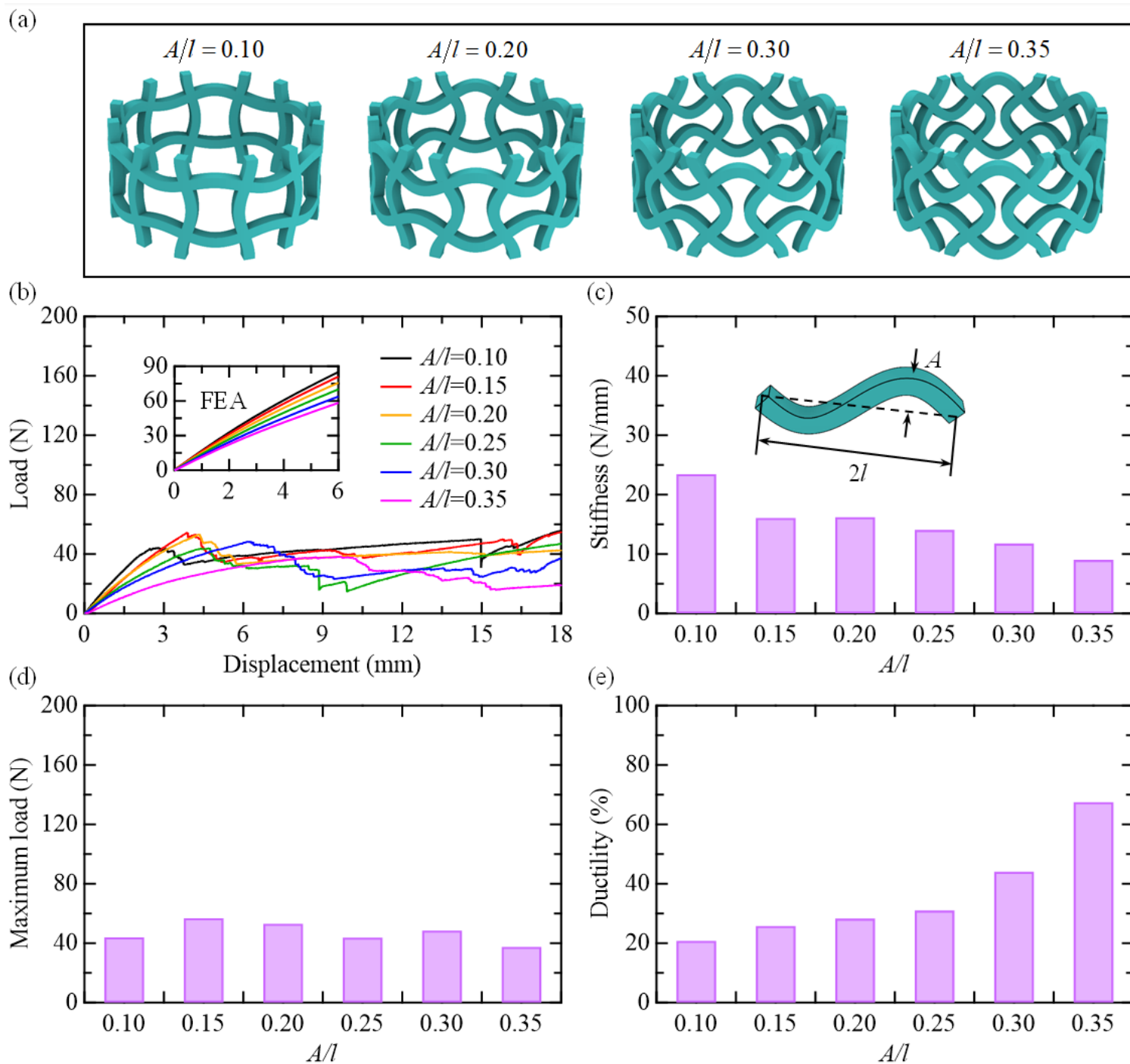


**Fig. 8.** Effect of amplitude on the performance of ATL. (a) RVEs with different beam amplitude. (b) Load-displacement curves. (c) Tubular lattice stiffness as a function of  $A/l$ . (d) Tubular lattice maximum load as a function of  $A/l$ . (e) Tubular lattice ductility as a function of  $A/l$ . Here,  $l = 7$  mm,  $D = 84/\pi$ ,  $t/l = 0.2$ ,  $h/l = 0.2$ .

**Figs. 9 (a) and (b)** show the deformation patterns for  $A/l = 0.1$  and  $A/l = 0.35$ , respectively. At the displacement of  $\delta = 3$  mm, fractures occur on the ligaments for  $A/l = 0.1$  as highlighted in the image, which accounts for the load drop in the load-displacement curve. However, no observable failure is found for  $A/l = 0.35$  at this stage, as evidenced by the smooth rising of load. At the displacement of  $\delta = 10$  mm, the fracture grows significantly. On the other hand,  $A/l = 0.35$  shows only mild failure, as shown in the highlighted area. This indicates significant ductile behavior of  $A/l = 0.35$ .

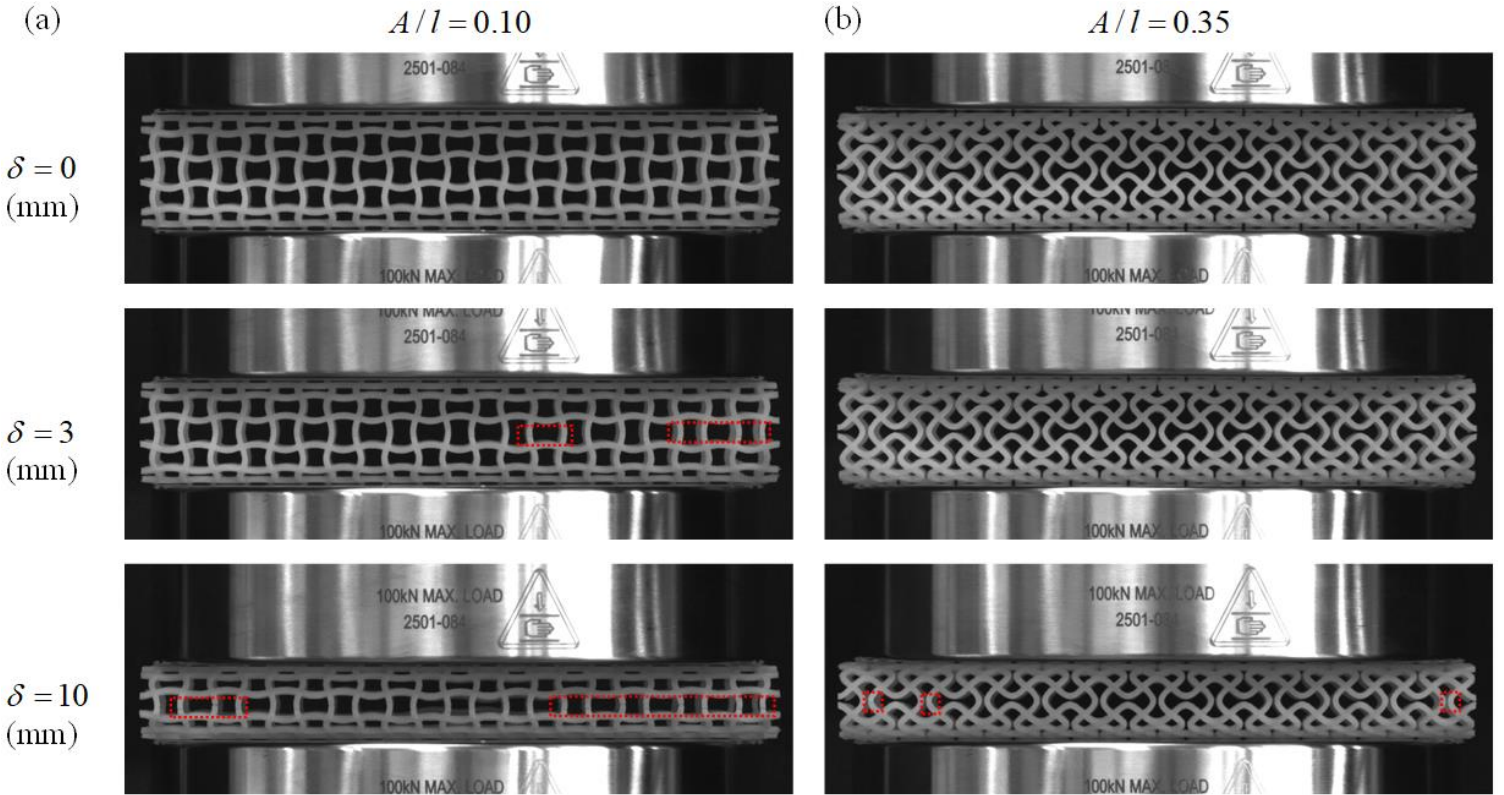


**Fig. 9.** Comparison of deformation patterns for ATL structure with different beam amplitudes. (a) Deformation patterns for  $A/l = 0.1$ . (b) Deformation patterns for  $A/l = 0.35$ .

#### 4. Conclusions

In summary, we have investigated the mechanical performance of a newly developed tubular lattice metamaterial under radial compression using an integrated experimental and numerical effort. Compared with conventional DTL structure, the proposed ATL design has superior ductility under large deformation. Our numerical simulations revealed the disparate stress distributions within the two configurations. The stress is concentrated on the joints of straight beams for DTL structure, while stress is more uniformly distributed on the sinusoidal ligaments for ATL structure. Intrinsically, this is due to the bending of sinusoidal ligaments along both radial and axial directions, which features more deformation space. In contrast, the straight beams are bent mainly along the radial direction. To explore the design flexibility of the proposed lattice metamaterials, we investigated the geometric features of beam ligament on the mechanical performance. We found that the beam depth  $h/l$  significantly affects the stiffness and peak load, while beam amplitude  $A/l$  influences the ductility extraordinarily. These parametric analyses can enable us to design ATL structures with prescribed radial performance, such as stiff yet ductile features. It should be pointed out, though, that we did not maintain the same relative density for the samples in the parametric studies. The difference of relative density will affect the relative values of mechanical properties. However, this difference has no effect in our findings and conclusions. As a preliminary study, we anticipate the proposed mechanically robust tubular architectures can be used as stents that will have a high potential for clinical translation to treat coronary and peripheral artery disease. Our ongoing work includes evaluation of the mechanical performance of this tubular lattice architecture with degradable constitutive materials and further optimizing the tubular architecture using inverse design approaches.

#### Author statement

Huan Jiang: Methodology, Formal analysis, Investigation, Data Curation; Hannah Ziegler, Zhennan Zhang, Heng Zhang, and Louise Le Barbenchon: Investigation, Data Curation, Writing - Original Draft; Sundar Atre and Yanyu Chen: Conceptualization, Writing - Review & Editing, Supervision. All authors have approved the final version of the manuscript.

## **Acknowledgments**

YC gratefully acknowledges the start-up fund from the Department of Mechanical Engineering at the University of Louisville.

## **Declaration of competing interest**

The authors declare that they have no known competing financial interests or personal relationships that could have appeared to influence the work reported in this paper.

## **Data availability**

The raw/processed data required to reproduce these findings cannot be shared at this time due to technical or time limitations.

## **References**

- [1] Hannan EL, Racz MJ, Arani DT, McCallister BD, Walford G, Ryan TJ. A comparison of short- and long-term outcomes for balloon angioplasty and coronary stent placement. *J. Am. Coll. Cardiol.* 2000;36(2):395-403.
- [2] Bart L, Dolmatch UB. Stent-Grafts: Current Clinical Practice. *Radiology.* 2000;217(1):94-94.
- [3] Wu W, Song X, Liang J, Xia R, Qian G, Fang D. Mechanical properties of anti-tetrachiral auxetic stents. *Compos. Struct.* 2018;185:381-92.
- [4] Palmaz JC. Balloon-expandable intravascular stent. *AJR.* 1988;150(6):1263-9.
- [5] Spencer B, King BM. Interventional Treatment of Coronary Heart Disease and Peripheral Vascular Disease. *Circulation.* 102(suppl\_4):Iv-81-Iv-6.
- [6] Wang Q, Fang G, Zhao Y-H, Zhou J. Improvement of Mechanical Performance of Bioresorbable Magnesium Alloy Coronary Artery Stents through Stent Pattern Redesign. *Appl. Sci.* 2018;8(12).
- [7] Shi W, Li H, Zhu T, Jin Y, Wang H, Yang J, et al. Study on the bending behavior of biodegradable metal cerebral vascular stents using finite element analysis. *J. Biomech.* 2020;108:109856.
- [8] Demanget N, Latil P, Orgéas L, Badel P, Avril S, Geindreau C, et al. Severe bending of two aortic stent-grafts: an experimental and numerical mechanical analysis. *Ann. Biomed. Eng.* 2012;40(12):2674-86.
- [9] Butany J, Carmichael K, Leong SW, Collins MJ. Coronary artery stents: identification and evaluation. *J. Clin. Pathol.* 2005;58(8):795-804.

- [10] Wong P, Leung WH, Wong CM. Migration of the AVE Micro coronary stent. *Catheter. cardiovasc. diagnosis.* 1996;38(3):267-73.
- [11] McGrath DJ, O'Brien B, Bruzzi M, McHugh PE. Nitinol stent design – understanding axial buckling. *J. Mech. Behav. Biomed. Mater.* 2014;40:252-63.
- [12] Grogan JA, Leen SB, McHugh PE. Computational micromechanics of bioabsorbable magnesium stents. *J. Mech. Behav. Biomed. Mater.* 2014;34:93-105.
- [13] Jacobs TS, Won J, Gravereaux EC, Faries PL, Morrissey N, Teodorescu VJ, et al. Mechanical failure of prosthetic human implants: a 10-year experience with aortic stent graft devices. *J. Vasc. Surg. Cases.* 2003;37(1):16-26.
- [14] Dumoulin C, Cochelin B. Mechanical behaviour modelling of balloon-expandable stents. *J. Biomech.* 2000;33(11):1461-70.
- [15] Cockerill I, See CW, Young ML, Wang Y, Zhu D. Designing Better Cardiovascular Stent Materials: A Learning Curve. *Adv. Funct. Mater.* 2021;31(1):2005361.
- [16] Zheng Q, Dong P, Li Z, Han X, Zhou C, An M, et al. Mechanical characterizations of braided composite stents made of helical polyethylene terephthalate strips and NiTi wires. *Nanotechnol. Rev.* 2019;8(1):168-74.
- [17] McGrath DJ, O'Brien B, Bruzzi M, Kelly N, Clauser J, Steinseifer U, et al. Evaluation of cover effects on bare stent mechanical response. *J. Mech. Behav. Biomed. Mater.* 2016;61:567-80.
- [18] Shang Z, Ma J, You Z, Wang S. Lateral indentation of a reinforced braided tube with tunable stiffness. *Thin-Walled Struct.* 2020;149:106608.
- [19] Grogan JA, Leen SB, McHugh PE. Comparing coronary stent material performance on a common geometric platform through simulated bench testing. *J. Mech. Behav. Biomed. Mater.* 2012;12:129-38.
- [20] Wang L, Chan Y-C, Liu Z, Zhu P, Chen W. Data-driven metamaterial design with Laplace-Beltrami spectrum as “shape-DNA”. *Struct. Multidisc. Optim.* 2020;61(6):2613-28.
- [21] García A, Peña E, Martínez MA. Influence of geometrical parameters on radial force during self-expanding stent deployment. Application for a variable radial stiffness stent. *J. Mech. Behav. Biomed. Mater.* 2012;10:166-75.
- [22] Han Y, Lu W. Optimizing the deformation behavior of stent with nonuniform Poisson's ratio distribution for curved artery. *J. Mech. Behav. Biomed. Mater.* 2018;88:442-52.
- [23] Lei M, Hong W, Zhao Z, Hamel C, Chen M, Lu H, et al. 3D Printing of Auxetic Metamaterials with Digitally Reprogrammable Shape. *ACS Appl. Mater. Interfaces.* 2019;11(25):22768-76.
- [24] Paxton NC, Daley R, Forrestal DP, Allenby MC, Woodruff MA. Auxetic tubular scaffolds via melt electrowriting. *Mater. Des.* 2020;193:108787.
- [25] Leonardi F, Graziosi S, Casati R, Tamburrino F, Bordegoni M. Additive Manufacturing of Heterogeneous Lattice Structures: An Experimental Exploration. *Proc. Int. Conf. Eng. Des.* 2019;1(1):669-78.
- [26] Cabrera MS, Sanders B, Goor OJGM, Driessen-Mol A, Oomens CWJ, Baaijens FPT. Computationally Designed 3D Printed Self-Expandable Polymer Stents with Biodegradation Capacity for Minimally Invasive Heart Valve Implantation: A Proof-of-Concept Study. *3D Printing and Addit. Manuf.* 2017;4(1):19-29.
- [27] Zaccaria A, Pennati G, Petrini L. Analytical methods for braided stents design and comparison with FEA. *J. Mech. Behav. Biomed. Mater.* 2021;119:104560.
- [28] Migliavacca F, Petrini L, Colombo M, Auricchio F, Pietrabissa R. Mechanical behavior of coronary stents investigated through the finite element method. *J. Biomech.* 2002;35(6):803-11.
- [29] Dolla WJS, Fricke BA, Becker BR. Structural and Drug Diffusion Models of Conventional and Auxetic Drug-Eluting Stents. *J. Med. Devices.* 2006;1(1):47-55.
- [30] Ruan X, Yuan W, Hu Y, Li J, Wu W, Xia R. Chiral constrained stent: Effect of structural design on the mechanical and intravascular stent deployment performances. *Mech. Mater.* 2020;148:103509.
- [31] Ahn BY, Shoji D, Hansen CJ, Hong E, Dunand DC, Lewis JA. Printed Origami Structures. *Adv. Mater.* 2010;22(20):2251-4.

- [32] Kuribayashi K, Tsuchiya K, You Z, Tomus D, Umemoto M, Ito T, et al. Self-deployable origami stent grafts as a biomedical application of Ni-rich TiNi shape memory alloy foil. *Mater. Sci. Eng. A*. 2006;419(1):131-7.
- [33] Javid F, Liu J, Shim J, Weaver JC, Shanian A, Bertoldi K. Mechanics of instability-induced pattern transformations in elastomeric porous cylinders. *J. Mech. Phys. Solids*. 2016;96:1-17.
- [34] Simons MF, Digumarti KM, Conn AT, Rossiter J. Tiled Auxetic Cylinders for Soft Robots. 2019 2nd IEEE International Conference on Soft Robotics (RoboSoft)2019.pp. 62-67.
- [35] Lee JW, Soman P, Park JH, Chen S, Cho D-W. A Tubular Biomaterial Construct Exhibiting a Negative Poisson's Ratio. *Plos One*. 2016;11(5):e0155681.
- [36] Guo Y, Zhang J, Chen L, Du B, Liu H, Chen L, et al. Deformation behaviors and energy absorption of auxetic lattice cylindrical structures under axial crushing load. *Aerosp. Sci. Technol*. 2020;98:105662.
- [37] Zhang XY, Wang XY, Ren X, Xie YM, Wu Y, Zhou YY, et al. A novel type of tubular structure with auxeticity both in radial direction and wall thickness. *Thin-Walled Struct*. 2021;163:107758.
- [38] Wu W, Tao Y, Xia Y, Chen J, Lei H, Sun L, et al. Mechanical properties of hierarchical anti-tetrachiral metastructures. *Extreme Mech. Lett*. 2017;16:18-32.
- [39] Luo C, Han CZ, Zhang XY, Zhang XG, Ren X, Xie YM. Design, manufacturing and applications of auxetic tubular structures: A review. *Thin-Walled Struct*. 2021;163:107682.
- [40] Hedayati R, Güven A, van der Zwaag S. 3D gradient auxetic soft mechanical metamaterials fabricated by additive manufacturing. *Appl. Phys. Lett*. 2021;118(14):141904.
- [41] Ren X, Shen J, Ghaedizadeh A, Tian H, Xie YM. A simple auxetic tubular structure with tuneable mechanical properties. *Smart Mater. Struct*. 2016;25(6):065012.
- [42] Hur JM, Seo D-S, Kim K, Lee JK, Lee KJ, Kim YY, et al. Harnessing distinct deformation modes of auxetic patterns for stiffness design of tubular structures. *Mater. Des*. 2021;198:109376.
- [43] Ansari M, Golzar M, Baghani M, Taghavimehr M, Abbasi Shirsavar M, Yahyavi M. An experimental investigation on shape memory polymer and metallic stents under bending and radial compression. *ERX*. 2020;2(4):045012.
- [44] Wu Z, Zhao J, Wu W, Wang P, Wang B, Li G, et al. Radial Compressive Property and the Proof-of-Concept Study for Realizing Self-expansion of 3D Printing Polylactic Acid Vascular Stents with Negative Poisson's Ratio Structure. *Materials (Basel, Switzerland)*. 2018;11(8).
- [45] ASTM D638-14 Standard test method for tensile properties of plastics. 2014.
- [46] Jiang H, Le Barbenchon L, Bednarczyk BA, Scarpa F, Chen Y. Bioinspired multilayered cellular composites with enhanced energy absorption and shape recovery. *Addit. Manuf*. 2020;36:101430.
- [47] Wong P, Leung Wh, Wong CmJC, diagnosis c. Migration of the AVE Micro coronary stent. 1996;38(3):267-73.
- [48] Pauck RG, Reddy BD. Computational analysis of the radial mechanical performance of PLLA coronary artery stents. *Med. Eng. Phys*. 2015;37(1):7-12.
- [49] Lee SE, Jeong MH, Kim IS, Ko JS, Lee MG, Kang WY, et al. Clinical outcomes and optimal treatment for stent fracture after drug-eluting stent implantation. *J. Cardiol*. 2009;53(3):422-8.
- [50] Jiang H, Zhang Z, Chen Y. 3D printed tubular lattice metamaterials with engineered mechanical performance. *Appl. Phys. Lett*. 2020;117(1):011906.

## Supplementary Information

### S1. Finite element simulation

The setup of finite element simulations for the radial compression of tubular lattice structure is shown in **Fig. S1**. To simulate the experiment of radial compression, two rigid plates were added to the top and bottom to ensure uniform deformation. Reference points were defined to apply the displacement in the simulation. All models in this work were meshed with 3D hexahedral element (C3D8). The ATL structure was meshed with 185,856 hexahedral elements, and the DTL structure was meshed with 276,804 hexahedral elements. General self-contact with friction coefficient of 0.25 was defined for tangential motion and hard contact for the normal direction.

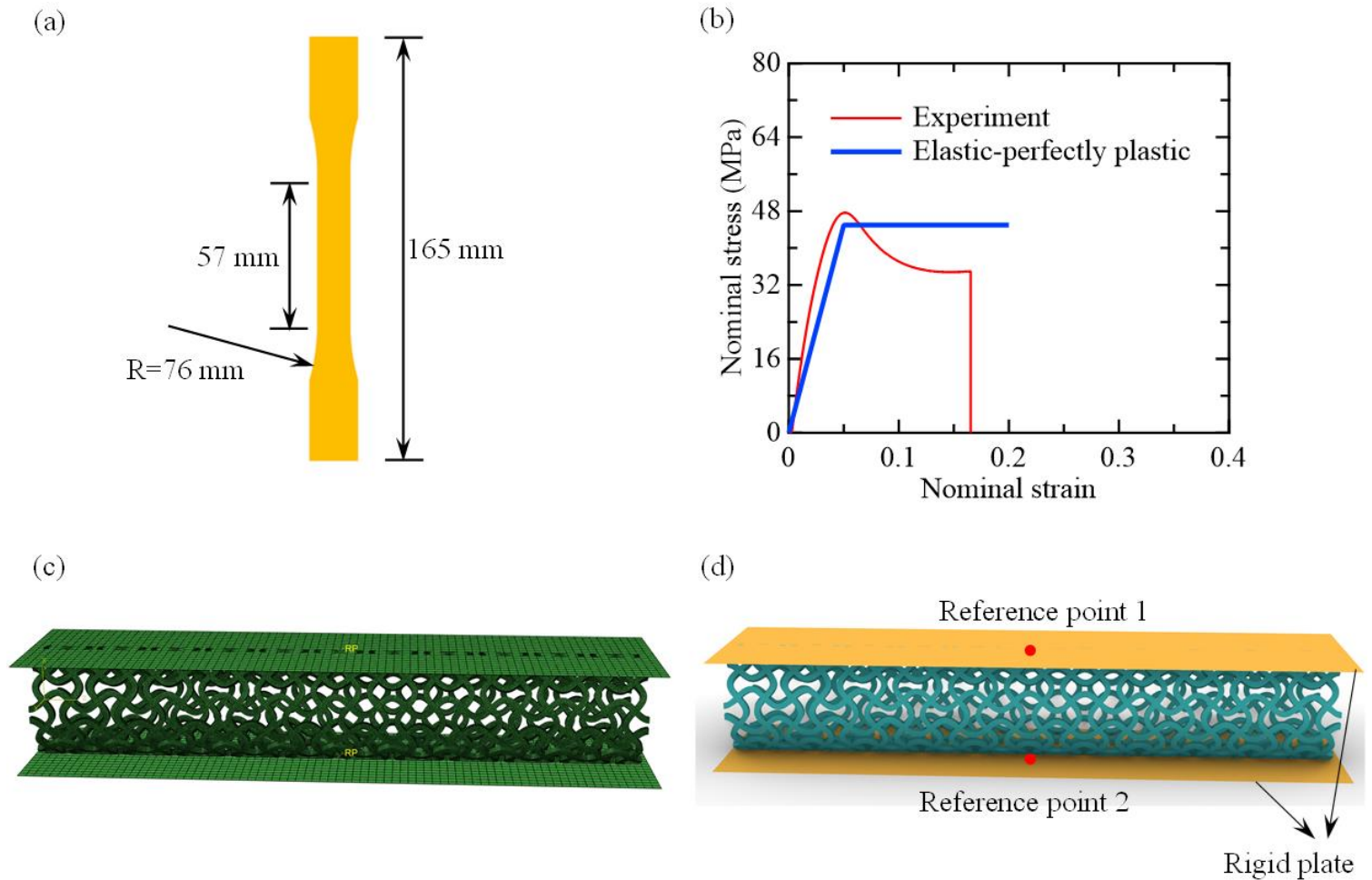


**Fig. S1** Tensile testing and finite element simulation setup. (a) Dumbbell-shape sample. (b) Stress-strain relation of experiment and simplified elastic-perfectly-plastic model. (c) Radial compression setup in Abaqus with rigid plates on the top and bottom. (d) Schematics of the ATL structure with rigid plates and reference points.

## **S2. Comparison of the proposed ATL and the conventional DTL structure**

The detailed comparison of contour plots of stress components is shown in **Figs. S2 (a)-(f)**. We can observe from **Figs. S2 (a)** and **(b)** that the stress component  $\sigma_{xx}$  is more uniformly distributed around the circumferential sinusoidal ligaments, while the straight beams of DTL design are featured by stress concentration of component  $\sigma_{xx}$  on the local joints. The stress component  $\sigma_{yy}$  for ATL is largely spread around the circumferential ligaments near the top and bottom region. However, the stress component is concentrated on the joints of straight beams for DTL near the top and bottom plates. On the other hand, stress component  $\sigma_{zz}$  spreads much more on the axial sinusoidal ligaments than the circumferential ones. Meanwhile, the magnitude of  $\sigma_{zz}$  is smaller than stress component  $\sigma_{xx}$  and  $\sigma_{yy}$ . In addition, the contour plot of displacement along axial direction, as shown in **Figs. S2 (g)** and **(h)**, reveals the effect of auxetic behavior, which shows that the sinusoidal ligaments flow toward the inside of the ATL structure, while the straight beams flow outside of the DTL structure. This unique feature leads to the bending of circumferential sinusoidal ligaments along both radial and axial directions. However, the straight ligaments of DTL structure bend mainly along the radial direction.

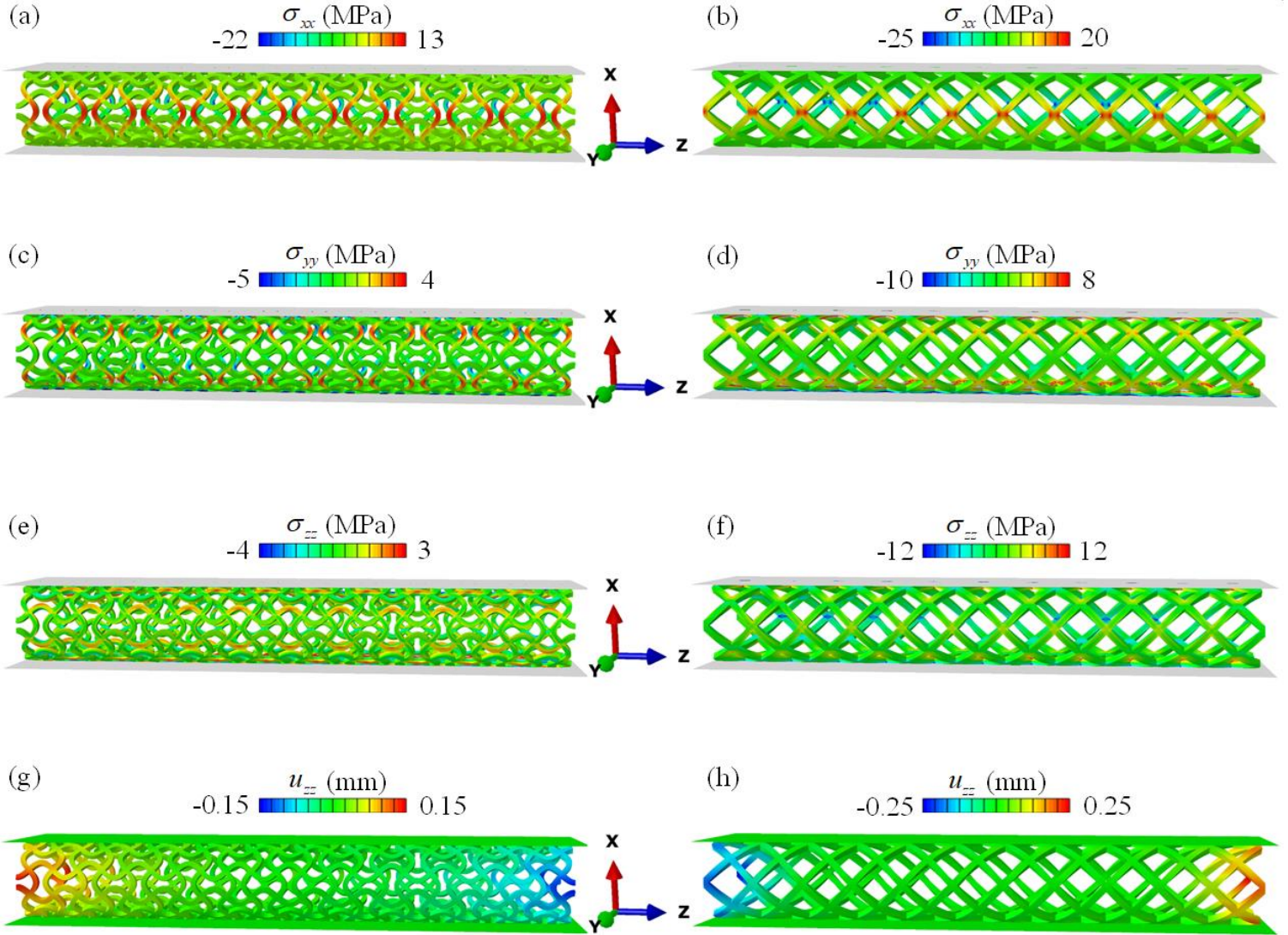


**Fig. S2.** Contour plots of stress components and displacement components under radial compression.

### S3. Effect of beam amplitude

To gain insights from a simulation point of view, we show the contour plots of Mises stress for different beam amplitudes in **Fig. S3**. The contour plots were exported from Abaqus using the same legend. With the increase of beam amplitude, the stress distribution exhibits more uniform pattern. Specifically, when  $A/l = 0.10$ , the stress is slightly more concentrated on the middle part of the circumferential ligaments. As the beam amplitude enlarges, the local stress concentration regions dissipate. As discussed in the main text, this contributes to the increasingly auxetic

effect when  $A/l$  augments. If the beam amplitude is small, the circumferential ligaments bend mainly along radial direction. However, if the beam amplitude is large, the auxetic effect will compel the circumferential ligaments to bend along axial direction as well.

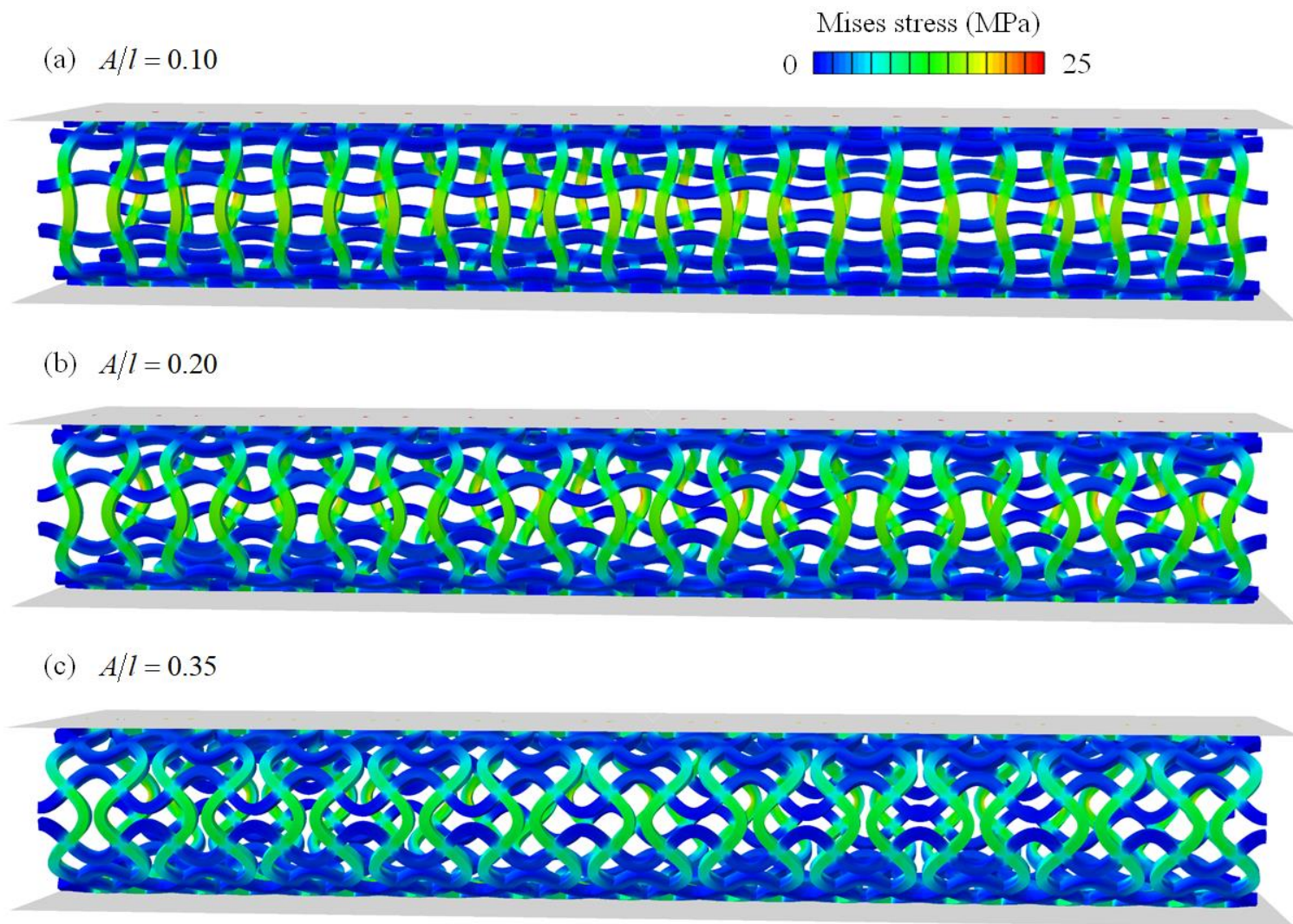


**Fig. S3.** Mises stress contour plots for different beam amplitudes.